ACADEMIC
PRESS

Available online at www.sciencedirect.com

SCIENCE DIRECT®

Journal of Sound and Vibration 261 (2003) 31–74

JOURNAL OF
SOUND AND
VIBRATION

www.elsevier.com/locate/jsvi

Flap-edge aeroacoustic measurements and predictions☆

Thomas F. Brooks*, William M. Humphreys Jr.

NASA Langley Research Center, Mail Stop 461, Hampton, VA 23681-0001, USA

Received 15 September 2000; accepted 3 May 2002

Abstract

An aeroacoustic model test has been conducted to investigate the mechanisms of sound generation on high-lift wing configurations. This paper presents an analysis of flap side-edge noise, which is often the most dominant source. A model of a main element wing section with a half-span flap was tested at low speeds of up to a Mach number of 0.17, corresponding to a wing chord Reynolds number of approximately 1.7 million. Results are presented for flat (or blunt), flanged, and round flap-edge geometries, with and without boundary-layer tripping, deployed at both moderate and high flap angles. The acoustic database is obtained from a small aperture directional array (SADA) of microphones, which was constructed to electronically steer to different regions of the model and to obtain farfield noise spectra and directivity from these regions. The basic flap-edge aerodynamics is established by static surface pressure data, as well as by computational fluid dynamics (CFD) calculations and simplified edge flow analyses. Distributions of unsteady pressure sensors over the flap allow the noise source regions to be defined and quantified via cross-spectral diagnostics using the SADA output. It is found that shear layer instability and related pressure scatter is the primary noise mechanism. For the flat edge flap, two noise prediction methods based on unsteady-surface-pressure measurements are evaluated and compared to measured noise. One is a new causality spectral approach developed here. The other is a new application of an edge-noise scatter prediction method. The good comparisons for both approaches suggest that the prediction models capture much of the physics. Areas of disagreement appear to reveal when the assumed edge noise mechanism does not fully define the noise production. For the different edge conditions, extensive spectra and directivity are presented. The complexity of the directivity results demonstrate the strong role of edge source geometry and frequency in the noise radiation. Significantly, for each edge configuration, the spectra for different flow speeds, flap angles, and surface roughness were successfully scaled by utilizing aerodynamic performance and boundary-layer scaling methods developed herein.
Published by Elsevier Science Ltd.

☆Paper based on that presented at the 6th AIAA/CEAS Aeroacoustics Conference as Paper AIAA-2000-1975, June 12-14, 2000, Lahaina, Hawaii.

*Corresponding author. Tel.: +757-864-3634; fax: +757-864-8290.
E-mail address: t.f.brooks@larc.nasa.gov (T.F. Brooks).

0022-460X/03/$ - see front matter Published by Elsevier Science Ltd.
PII: S0022-460X(02)00939-2

1. Introduction

Airframe noise can be dominant during airport approach and landing when the engines are at low-power and the high-lift systems and landing gears are deployed. This becomes particularly true as present-day propulsive systems become quieter [1]. As a result, there has been an increased emphasis placed on the measurement and modelling of non-propulsive components such as flaps, slats, and undercarriage.

As reviewed by Crighton [2], a number of studies of airframe noise were conducted in the 1970 s and early 1980s. An early evaluation was performed by Hardin [3]. Empirical airframe noise studies and prediction developments include those of Fink [4] and Fink and Schlinker [5]. A series of airfoil self-noise experiments were performed by Brooks and Hodgson [6] and Brooks and Marcolini [7–9] for trailing edge noise and wing tip noise. The results of these studies formed the basis of a comprehensive self-noise prediction method [10] for isolated airfoils. As part of a wing and flap high-lift system, the flap is much more loaded aerodynamically than it would be if isolated. Because of this, it has been found capable of producing much more intense noise. Block [11] in wing, flap, and landing gear interaction studies found flaps to contribute significantly to the overall noise. Kendall [12] and Kendall and Ahtye [13], using an elliptical acoustic mirror, found strong localized flap-edge noise. This was confirmed by Fink and Schlinker [5] in component interaction studies. McInerny et al. [14], Ahtye et al. [15], and Miller and Meecham [16] performed cross-correlation studies between unsteady surface pressures and noise field measurements for the tip region of an isolated wing, single slotted flap, and triple slotted flaps, respectively. The side edges of the multiple flaps were found to significantly exceed other airframe noise sources [16].

The 1990s produced an increase in airframe noise research activity [17], particularly due to the NASA Advanced Subsonic Technology (AST) program. Several tests are particularly notable. A 4.7% scale DC-10 aircraft model was tested in the NASA Ames 40×80 ft wind tunnel, as reported by Bent et al. [18], Hayes et al. [19] and Guo et al. [20,21]. Inflow microphones, a phased-microphone array, and a parabolic mirror directional microphone system were used along with unsteady surface pressure sensors on inboard and outboard flaps. The flap-edge noise was found to dominate other noise sources. Significant correlations were found between edge pressures and the measured noise [21]. Noise reduction concepts were evaluated [22]. A series of tests of a large unswept wing (2.5 ft chord) and half-span Fowler flap were conducted in the NASA Ames 7×10 ft wind tunnel, as reported by Storms et al. [23], Horne et al. [24], and Storms et al. [25]. The tests provided basic aerodynamic data and, although the tunnel was hard-walled, limited acoustics were obtained using large phased arrays of microphones. A computational study by Khorrami et al. [26] provided substantial agreement with the data. This was used to examine two possible noise source models, namely, a vortex-instability model and a shear layer vortex-sheet model.

The present paper concerns a wing and flap model tested in the quiet flow facility (QFF) at NASA Langley. The model is a NACA 63_2-215 wing with a 30% chord half-span Fowler flap. This is the same as that used in the aforementioned 7×10 ft wind tunnel test at NASA Ames, except here the model is about one half the size. As reported by Macaraeg [17], this model in the QFF has provided the means to closely examine the aerodynamic and acoustic physics for slats and flaps. Measurements of the flow field in the QFF, by Radezrsky et al. [27] included hot wire, hot film, 5-hole probe surveys, laser light sheet, and flap surface oil flows. These measurements revealed a dominant flap vortex structure resulting from the merger of two upstream vortices—one strong vortex, formed from the pressure side to around the flap edge, and a weaker vortex formed at the flap side edge on the suction side. In the vicinity of the trailing edge, the vortex is far removed from the flap surface. Computational efforts by Khorrami et al. [28] and Takallu and Laflin [29] using Reynolds Averaged Navier–Stokes solutions (RANS) duplicated the key mean features of the edge flow. Streett [30] developed a computation framework for the simulation of the fluctuating flow field associated with this complex flap-edge vortex system. Streett's computations, utilizing a calculated mean flow field [28], further crystallized the shear layer instability and vortex-instability disturbance models [26] for noise production. Linear stability analysis determined dominant frequency ranges of unstable flow disturbances [31]. Guo [32,33], in a similar time frame, followed with a semi-analytical and semi-empirical prediction model of this shear layer instability mechanism. Predictions from this model compared well with flap-edge noise data when certain scale parameters were used.

The initial aeroacoustic measurements for an instrumented version of the above model tested in the QFF were presented by Meadows et al. [34]. Measurements included flap-edge noise-source location mapping by a large directional (phased) microphone array system, flap-edge noise spectra and directivity by a smaller array, and cross-spectra between unsteady surface pressure sensors about the flap edge. Details of the microphone array design and methodology used in the testing was presented by Humphreys et al. [35]. Microphone array testing methodology was refined and quantified using the QFF systems, as reported by Brooks and Humphreys [36]. The present study builds upon this work.

In this study, the generation and radiation of flap-edge noise for the flat (or blunt), flanged, and round flap-edge configurations are examined. The basic flow pattern about the edge is studied using computational fluid dynamic (CFD) calculations and measured static pressure distributions. Simplified flow calculations are then developed to provide key aerodynamic parameters needed for noise prediction and scaling. Cross-spectral amplitude and phase between unsteady surface pressure sensors over the flap-edge surface are analyzed to reveal the character of the hydrodynamic pressure field due to turbulent flow and the nearfield flap-edge noise generation. coherent output power (COP) spectra diagnostics using the measured pressures and the noise provide a measure of the noise source distribution along the flap edge. The noise source thus determined is examined for consistency with the previously mentioned shear layer instability mechanism [26,30,33]. For the flat edge flap, separate noise prediction methods are developed and validated from (1) a causality approach that connects the noise to the cross-spectra between the surface pressure and far field noise through fundamental aeroacoustic formulations and (2) an edge-noise scatter solution. Both methods utilize the surface pressure measurements on the suction and pressure sides near the flap edge. Next, the noise spectra and directivity are presented for three edge configurations for different surface roughness, flap angles, and flow speeds. The spectra are then examined for scalability for each configuration using flap mean lift and boundary-layer thickness descriptions.

2. Test setup and method

2.1. Test apparatus

The test model apparatus is shown mounted in the quiet flow facility (QFF) in Fig. 1. The QFF is a quiet open-jet facility designed for anechoic acoustic testing. For the present airframe model testing, a 2×3 ft rectangular open-jet nozzle is employed. The model is a NACA 63_2-215 main-element airfoil (16 in chord and 36 in span) with an attached half-span Fowler flap (4.8 in chord). The flap is attached by an adjustable set of "U" brackets to minimize bracket interference with the ideal flap flow field. The model is held in place by vertical side plates, which are themselves rigidly mounted to side plate supports of the nozzle. In the photo, the model is visible through the plexiglas windows located on the side plates. The main element airfoil and flap are instrumented with static pressure ports and unsteady pressure sensors [34].

A view of the main element and flap in the vicinity of the flap edge is sketched in Fig. 2. The flat edge flap is shown accompanied by edge modifications. When attached, the flange edge produces a cavity depth of 1/8 in. The flange thickness is 0.05 in. The round edge attachment is a half-circle cross-section shape that matches the airfoil contour. The effect of surface roughness on the flap-edge noise was examined by applying grit. For the flat edges, 60 grit at a density of about 70 particles/in^2 was applied on the edge and both suction and pressure side surfaces over a 2 in span. For the round edge, 120 grit at about 800 particles/in^2 was applied, but was restricted to one-half of the round edge surface area—towards the flap's pressure side. The intent of the grit was to produce thickened and well-developed turbulent boundary layers in the vicinity of the side edge. For this paper, the main element angle was set at 16° with respect to the tunnel centerline and two flap angles were $\alpha = 29°$ and 39°, with respect to the main element. A main element angle of 20°

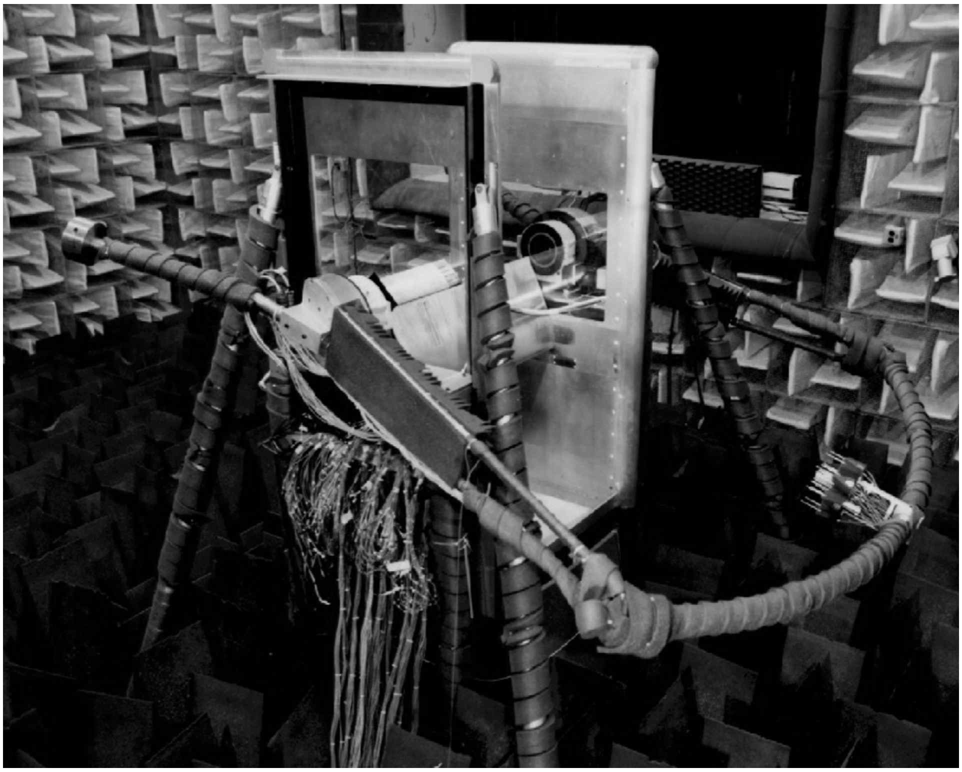

Fig. 1. Test apparatus with SADA mounted on pivotal boom in QFF.

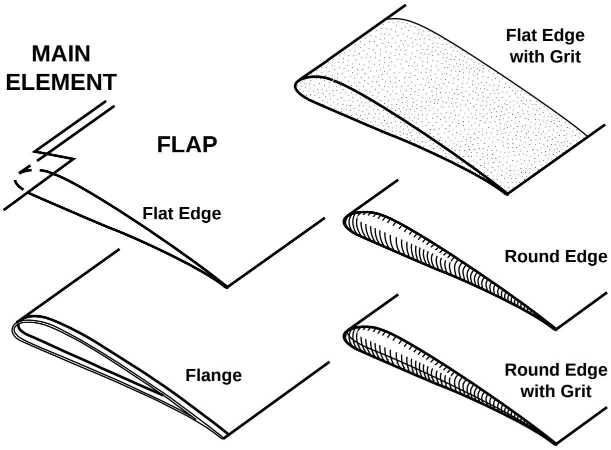

Fig. 2. Sketch of flap edge treatments.

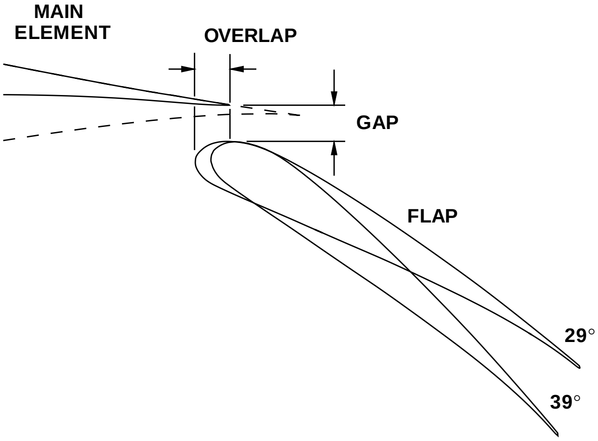

Fig. 3. Flap and gap geometry. Gap and overlap for 29° flap angle are 0.0227 and 0.0242, respectively, as normalized to the main element chord length. For 39°, these are 0.0231 and 0.0132, respectively.

was also tested, but as will be indicated in the next section, the flap test results depended almost completely on the flap angle itself. The gap and overlap settings for these two flap angles are shown in Fig. 3. The positions of the flush-mounted unsteady pressure sensors in the flap-edge vicinity are shown in Fig. 4. The chordwise distance from the leading edge is x and the spanwise distance from the side edge is y. As will be discussed, the sensors of present interest are those on the pressure and suction surface. These sensors are Kulite model LQ-34-064-5A. They are aligned spanwise at 0.06, 0.81, and 1.81 in (sections A, B, and C, respectively) from the edge. The chordwise position for each sensor is given in Table 1.

The far field acoustics of the model are measured by small aperture directional array (SADA) [35,36], which is seen in Fig. 1 to be mounted on a pivotal boom positioned by rotational stepping motors. The SADA is always 5 ft from the center of the main element trailing edge. It consists of

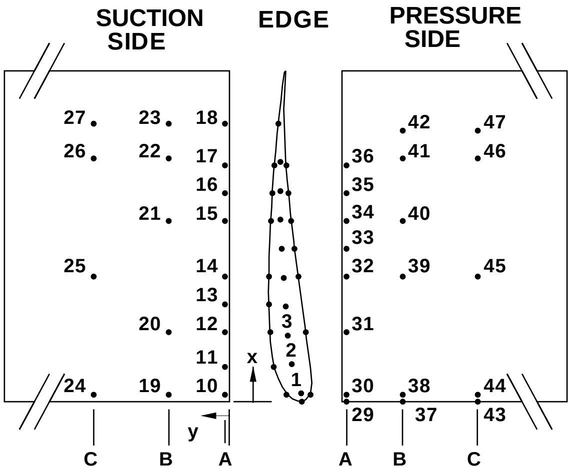

Fig. 4. Drawing of unsteady surface pressure sensor distribution.

Table 1
Pressure sensor co-ordinates

Sensor co-ordinates							
No.	*x* (in)	No.	*x* (in)	No.	*x* (in)	No.	*x* (in)
10	0.12	20	0.95	30	0.12	39	3.02
11	0.54	21	2.62	31	0.95	40	2.18
12	0.95	22	3.45	32	1.78	41	1.35
13	1.37	23	3.99	33	2.20	42	0.93
14	1.78	24	0.12	34	2.62	43	4.80
15	2.62	25	1.78	35	3.03	44	4.68
16	3.03	26	3.45	36	3.36	45	3.02
17	3.36	27	3.99	37	0.00	46	1.35
18	3.99	29	0.00	38	0.12	47	0.93
19	0.12	—	—	—	—	—	—

$y_A = 0.06$ in, $y_B = 0.81$ in, $y_C = 1.81$ in.

33 B&K 1/8 in microphones projecting from an acoustically treated metal frame. The aperture of the array is small, with a maximum diagonal aperture of 7.76 in. The small size reduces bias error by locating all the microphones in the array within approximately the same source directivity, regardless of SADA's elevation or azimuth position about the model. In Fig. 5, the SADA measurement positions are drawn in a side view (opposite side to that of Fig. 1) of the test setup. The SADA is shown located in a plane perpendicular to and centered on the span of the model, corresponding to zero azimuthal angle ($\psi = 0°$). The position of SADA in the photo of Fig. 1 corresponds to an elevation angle $\phi = -124°$ in the drawing. In Fig. 5, the SADA is seen positioned at $\phi = 107°$, on the pressure side of the model. The open-jet shear layer boundaries (defined at 10% and 90% of the potential core velocity) are shown as measured along the $\psi = 0°$

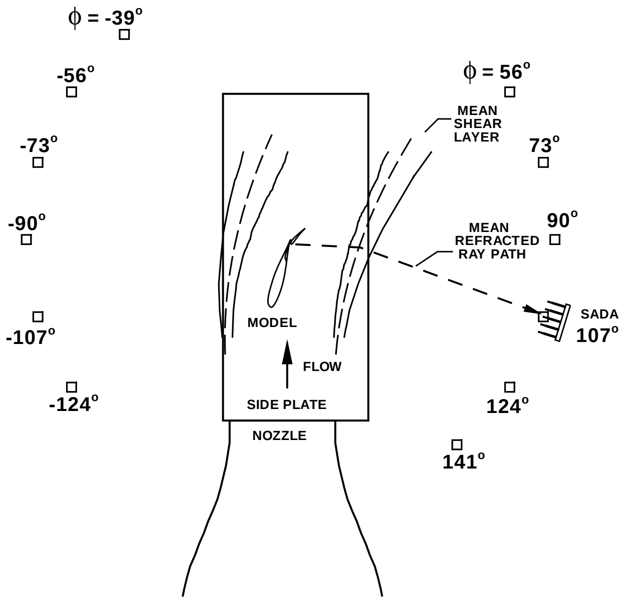

Fig. 5. Sketch of test setup. The noise ray path from the flap edge to the SADA is illustrated.

plane. The SADA position at $\phi = 56^\circ$ was near the limit of where intermittent shear layer turbulence would disrupt the acoustic measurements. A mean shear line is shown, which is part of a curved three-dimensional mean shear surface defined mathematically from the shear layer measurements. This is used in SADA processing to determine shear layer refraction corrections. The drawing illustrates the refracted noise ray path from the flap-edge source region to the microphone.

2.2. Data acquisition and post-processing

The array microphones and surface pressure sensors employed acquisition hardware consisting of transient data recorders controlled by a workstation. All 35 microphone channels (including two reference microhones) were recorded with a 14-bit dynamic range, simultaneously sampled with 32 pressure sensor channels using a 12-bit range, at a sampling rate of 142.857 kHz. Two million 2-byte samples were taken for each acquisition. The microphone signals were high pass filtered at 300 Hz. All channels had anti-aliasing filters set at 50 kHz, which is substantially below the 71.43 kHz Nyquist frequency.

Microphone and pressure sensor calibration data were accounted for in the post-processing. For the SADA microphones, regular pistonphone and injection calibrations of amplitude and phase were made. Amplitude and phase calibrations for the pressure sensors employed a miniature speaker-driver capable of high-frequency output. The measured outputs were referenced to the output of a 1/8 in B&K Model 4133 microphone. (The high-frequency outputs of the present Kulite sensors are unfortunately limited. In this report, surface pressure spectral data is limited generally to 13.5 kHz, where flat frequency response and signal to noise are good.) Initial post-processing of the test data begins with the computation of the cross-spectral matrix for each data set. The computation of the individual matrix elements is performed using fast fourier transforms (FFT) of the original data ensemble. All data are segmented into 1000 non-overlapping blocks each containing 2^{12} samples, yielding a frequency resolution of 34.88 Hz. A Hamming window is used.

A conventional beamforming approach, employing matrices of cross-spectra between the array microphones [35,36], is used to electronically “steer” the array to chosen noise source locations. The processing accounts for mean amplitude and phase changes due to refracted sound transmission through the shear layer to the individual microphones of the arrays. A mean refracted ray path is illustrated in Fig. 5. The correction terms are calculated [33] using Snell’s law in Amiet’s method [37], modified to account for a curved three-dimensional mean shear surface defined in the shear layer. A key feature of the array processing is that spatial resolution (or sensing area over noise source regions) can be controlled independently of frequency and steering-direction over broad frequency ranges. The microphone shading algorithms methodology used is adapted from Refs. [38,39] and evaluated with respect to the present test in Refs. [35,36]. Note that for each test case, the cross-spectral matrix has a corresponding background matrix subtracted from it to remove extraneous system noise (measured microphone and sensor noise for zero tunnel flow speed). The array processing references levels to an equivalent single microphone measurement. Spectra data are determined for each narrowband frequency (34.88 Hz resolution bandwidth) of interest. Other spectral bandwidths that are presented in this paper are formed from the narrowband spectra.

3. Flap-edge flow field

In this section, the basic flap-edge flow is examined with respect to parameters required to evaluate the unsteady surface pressures and related noise field.

3.1. Basic aerodynamics

Extensive aerodynamic measurements for the present model have been reported by Radezrsky et al. [27]. The model was shown to function as a high-lift device, with the main element and flap properly interacting aerodynamically. The elements are close enough that the flow acceleration about the leading edge of the flap significantly reduces the required pressure recovery at the main element trailing edge, but the elements are separated sufficiently so that the viscous boundary layers do not merge. This increases the overall lift, especially on the main element, compared to lifts obtainable separately. The QFF facility produces a maximum Mach number of 0.17 for this model configuration, which corresponds to a main element chord Reynolds number of 1.7×10^6. In order to maintain attached flow on the flap, the boundary layer transition was fixed by serrated tape applied to the lower surface of the main element at 30% chord and on the leading edge of the flap. Pressure coefficient plots revealed very similar performance to the somewhat larger Reynolds number conditions of the similar model [23] tested in the Ames closed wall 7 × 10 ft tunnel. In the QFF, the flap angle with respect to the main element was $\alpha = 29^\circ$ and 39°, whereas the main element was set at 16° and 20° angle of attack to the tunnel centerline. (Note that 16°, for the main element, is approximately equivalent to an angle of attack of about 5° in the closed wall tunnel.)

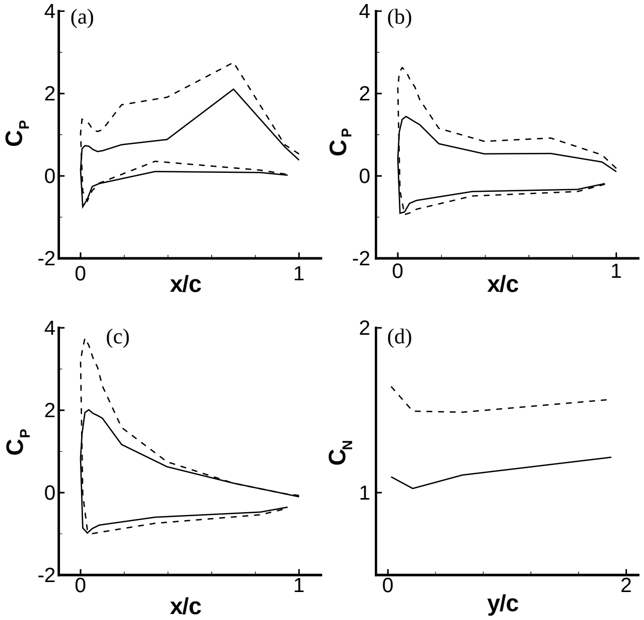

Fig. 6. Pressure coefficient distributions over x/c for (a) $y/c = 0.0271$, (b) $y/c = 0.2083$, and (c) $y/c = 1.875$. Normal force coefficient distribution over y/c in (d). Keys for flap angles α are: ——, 29°; – – –, 39°.

The flap flow field was found to be dictated almost entirely by the flap angle, which is measured with respect to the main element, and not the main element angle.

For the present QFF testing, pressure and lift distributions for the flap are presented in Fig. 6. The main element angle was 16°. The gap and overlap settings, shown in Fig. 3, differ only slightly from those of Ref. [27]. Static pressure coefficient distributions at three spanwise locations of the flap are shown in Fig. 6 for the tunnel Mach number $M_0 = 0.17$ for the two α values. The spanwise cuts are shown for $y/c = 0.027$, 0.208, and 1.875. The ratio y/c is the distance from the flap edge compared to the flap chordlength c. At $y/c = 1.875$, at the center of the flap section, the expected two-dimensional lift distribution behavior with high suction peaks is shown for both angles. As y/c decreases (meaning the flap side is approached), the high suction peak at the forward (leading edge) stations are reduced and the pressure differential diminishes. Near the side edge, a low-pressure region exists at a downstream section of the chord, which is due to a strong vortex being formed on the suction side. Also shown in Fig. 6 is the normal force (normal to chordline) coefficient C_N, with respect to c, versus y/c. An additional y/c location of 0.625 is represented here. It is seen that the sectional lift is diminished as the side edge is approached except for an increase very near the edge due to the presence of the strong vortex on the suction surface. At the inboard station $y/c = 1.875$, $C_N = 1.213$ and 1.567 for $\alpha = 29°$ and 39°, respectively. The ratios of C_N and α values show almost a linear dependence of lift to flap angle.

The vortex found on the suction surface near the flap edge was shown in Ref. [27] to be a result of the strong primary vortex and a weaker vortex merging. The primary vortex is formed along the pressure side (bottom) edge and grows in size in the streamwise direction, and a weaker vortex is formed near the suction surface edge. Steady RANS computations of Ref. [28] found agreement with the basic measured features of the merger of the dual vortex system and the general location of the resultant vortex. For both the experiment and calculations, the vortex bursts above the suction side surface for the 39° flap angle case [28], although this is not evident for the near-surface flow field represented in Fig. 7. The bursting occurs when the local flow angularity is too high or the axial velocity component is too low to maintain a tight potential-vortex core. Fig. 7 shows portions of the RANS solutions for the two flap angle QFF test cases of the present study. The contours show lines of constant static pressure on the surface. Intervals between the lines correspond to intervals in C_p of 0.346. The two component vectors shown are the calculated velocities over a projected surface defined at 0.035 in (approximately a boundary-layer thickness) above the suction and pressure surfaces. Only the edge velocity vectors from the pressure side are seen because of the oblique view of Fig. 7. The flow about the side-edge surface is omitted for clarity. The vector pattern clearly shows the presence of the resultant vortex and its strong

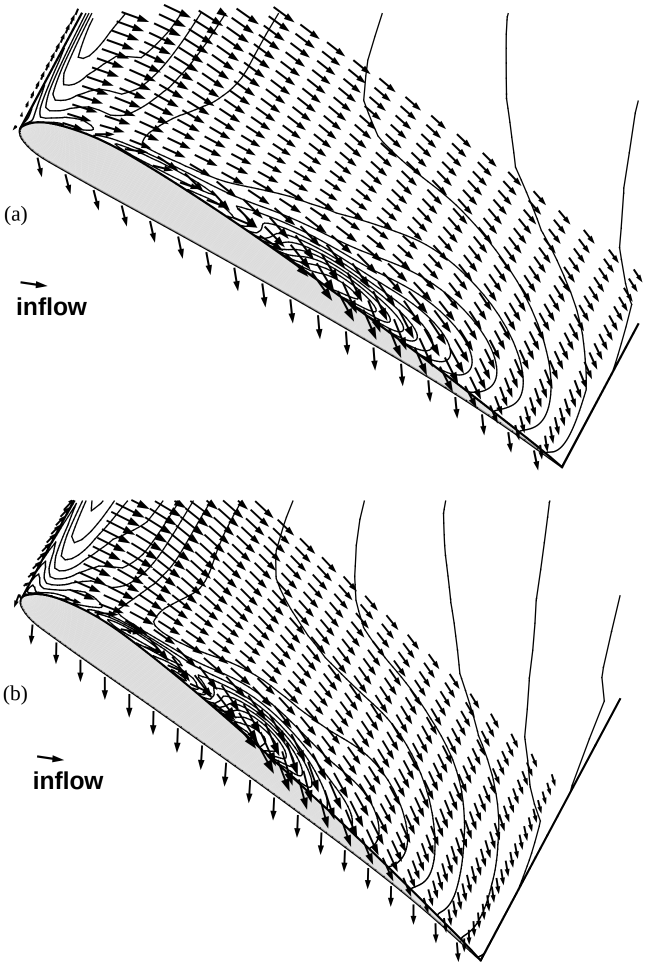

Fig. 7. CFD results of flap-edge-flow velocity vectors in planes parallel to and 0.035 in above the surface. The flap angles α are: (a) 29° and (b) 39°. The inflow $M_0 = 0.17$.

influence on the flap-edge flow field. The vortex is trailed downstream of the model, but the vectors show the formation of the vortex is essentially attached at the top (suction) edge surface. The attachment is seen to be just aft of mid-chord for the 29° flap angle case, but slightly forward of mid-chord for the 39° flap angle. The vortex strength is mostly defined by the strong sheared flow velocity across the pressure surface edge which wraps around the vortex and "feeds" it.

Of primary interest for this study are flow parameters that provide guidance in determining noise sources and provide pertinent input to prediction theory. If the flap-edge noise problem is indeed an edge scattering problem, one would view the boundary layer character and associated velocities as primary parameters. One should be able to tie these to surface pressure data to validate the noise source–somewhat similar in approach to that done in Ref. [6] for trailing edge noise. We direct our attention to the edge pressure sensors on the suction and pressure sides. These would be the only sensors in the strong edge flow field and, at the same time, be in the near field of such a scattering phenomenon. They should therefore be representative of the source region. Note that the flap side-edge surface, between the suction and pressure sides, has generally lower velocity and its sensors (1 through 9) are not considered here as representative of the source region (although they are in the near field of such scatter). In Table 2, for the sensors indicated, values are given for the near boundary-layer thickness δ, the corresponding Mach number M_c, and flow angle β_c, determined over planes parallel to the surface and at height $z = \delta$ above the surface. The choice of δ is partially subjective. It corresponds to the outer edge of the shear flow nearest the surface. An illustration of the velocity field $U(z)$ above an edge sensor is shown in Fig. 8. The top view shown defines the angle β_c from the normal to the edge. The subscript

Table 2
Calculated edge flow boundary-layer thickness and velocity values

	CFD values (simple model values) for $M_0 = 0.17$					
	$\alpha = 29°$			$\alpha = 39°$		
Sensor no.	δ (in)	M_C	β_C (deg)	δ (in)	M_C	β_C (deg)
10	0.010	0.21 (0.222)	77 (90)	0.020	0.22 (0.237)	82 (90)
11	0.010	0.21 (0.222)	90 (90)	0.012	0.27 (0.237)	82 (90)
12	0.010	0.23 (0.222)	85 (90)	0.025	0.29 (0.237)	68 (90)
13	0.030	0.22 (0.222)	73 (90)	0.050	0.265 (0.237)	80 (90)
14	0.050	0.24 (0.222)	82 (90)	0.050	0.33 (0.237)	76 (90)
15	0.030	0.35 (0.285)	54 (51)	0.045	0.32 (0.331)	43 (46)
16	0.040	0.33 (0.285)	48 (51)	0.045	0.30 (0.331)	46 (46)
17	0.050	0.31 (0.285)	52 (51)	0.060	0.28 (0.331)	60 (46)
18	0.120	0.25 (0.285)	58 (51)	0.150	0.24 (0.331)	65 (46)
30	0.010	0.13 (0.215)	28 (34)	0.025	0.15 (0.253)	10 (24)
31	0.020	0.19 (0.215)	38 (34)	0.020	0.205 (0.253)	28 (24)
32	0.020	0.21 (0.215)	35 (34)	0.020	0.205 (0.253)	26 (24)
33	0.025	0.22 (0.215)	33 (34)	0.025	0.205 (0.253)	25 (24)
34	0.030	0.22 (0.215)	32 (34)	0.030	0.22 (0.253)	25 (24)
35	0.030	0.22 (0.215)	31 (34)	0.030	0.21 (0.253)	25 (24)
36	0.030 ($\delta = 0.0453$)	0.20 (0.215)	32 (34)	0.030 ($\delta = 0.0314$)	0.205 (0.253)	27 (24)

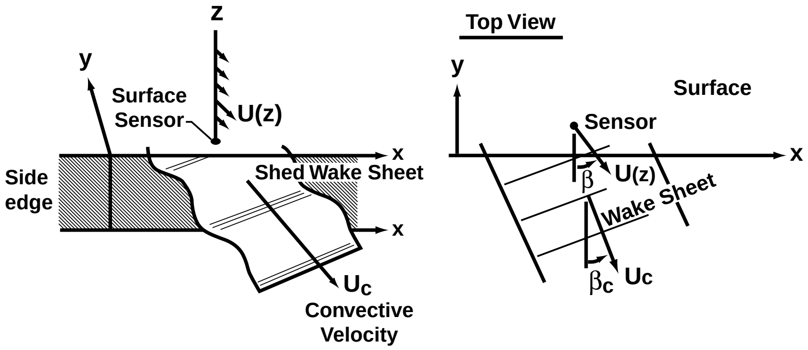

Fig. 8. Flow above a surface sensor and an idealized shed instability wave geometry at edge of flap.

designation c (for convective) is used to indicate the flow above the sensors is assumed to also represent any moving disturbance or flow structure that may cause noise-producing pressure scatter at the edge. The hypothesized convecting wake sheet illustrated in Fig. 8 will be subsequently discussed.

For both flap angle cases considered, Table 2 indicates that δ, M_c, and β_c remains generally invariant along much of the pressure side edge. The flow speed M_c, as well as the cross-flow (or spanwise) component of velocity $M_c \cos \beta_c$, exceed the tunnel value of $M_0 = 0.17$ over most of the chord. On the aft (downstream of mid-chord) suction side edge, where the attached vortex flow comes off the surface past the edge, the flow velocities are high, reaching up to about twice the free-stream value. Forward on the suction side edge, the velocities are lower than those aft and the cross-flow diminishes greatly with flow skew angle β_c approaching 90°. An unexpected result, to the present authors, for the CFD flow field is the lack of anticipated changes in δ and M_c values with changes in flap angle. Expected increases in M_c did not occur with increased flap angle, even in regions further away from the surface. It should be mentioned that Ref. [28] noted that the solutions, while remarkably good overall in defining basic flow features, found disagreements with measured velocities on the order of 10–15%. Concerns about the thickness of the shear layer were also expressed. It was suggested in Ref. [28] that improvements may be needed with regard to grid resolution and turbulence modeling. Because of the importance of these parameters to the present effort, alternate calculations are made and are presented in the following section. The CFD solution, however, is utilized in providing a reference for primary flow field features.

3.2. Simplified edge flow calculations

Simple aerodynamic modeling is used here to take into account Reynolds number and flap angle effects in the definition of boundary-layer thickness and velocity values. This complements the description of the complex three-dimensional flow field given by the CFD solution.

From thin airfoil theory [40], the sectional lift per unit span L' equals

$$L' = \rho U_0 \Gamma = \rho U_0 \int_0^c \bar{\gamma}\, \mathrm{d}x = q_0 c C_N, \tag{1}$$

where ρ is the medium density and Γ is the airfoil circulation given an incoming stream velocity of U_0. The circulation density $\bar{\gamma}$ of the vortex sheet defines the airfoil in the stream from the leading edge at $x = 0$ to the trailing edge at c, where c is the chordlength (of the flap in the present case). The dynamic pressure is $q_0 = \rho U_0^2/2$ and C_N is the sectional lift coefficient defined by Eq. (1). Fig. 9(a) shows a sketch of an inboard section of the flap where the flow is essentially two dimensional. The velocity jump across the airfoil sheet is $\bar{\gamma}(x) = u_{su} - u_{pr}$, where u_{su} is the velocity along the suction side and u_{pr} is that along the pressure side. The mean or average velocity jump over the chord is $(u_{su} - u_{pr})_{mean} = U_0 C_N/2$. The average values of u_{su} and u_{pr} are thus

$$(u_{su})_{mean} = U_0(1 + C_N/4), \quad (u_{pr})_{mean} = U_0(1 - C_N/4). \tag{2}$$

Along with the streamwise flow component above, the cross-flow component is required to estimate the edge flow. For this purpose, Fig. 9(b) illustrates a somewhat heuristic flap vortex model, where the bound circulation of strength Γ of the flap is transitioned to a trailed wake vortex of the same strength at the edge. Fig. 9(c) shows a forward section view (cut A′ in Fig. 9(d)) where the vortex of core radius r_0, is "drawing" fluid at velocity u_v from the pressure side into itself. It is assumed that the vortex does not greatly affect the edge flow on the upper suction side at this section. (Note that any contributions from "secondary" vortices are ignored.) For the aft section (cut B′) flow, the same basic vortex 'draws' fluid at the same velocity u_v from both the pressure and suction sides. The maximum velocity of the vortex is at the core radius and equals u_v. The velocity description chosen for the vortex is the Scully model [41,42] which distributes the circulation to simulate the effects of viscosity. The velocity due to the vortex is given in terms of the radius r from the center; $u = (\Gamma/2\pi r)[r^2/(r^2 + r_0^2)]$. (For an ideal point vortex, the bracketed

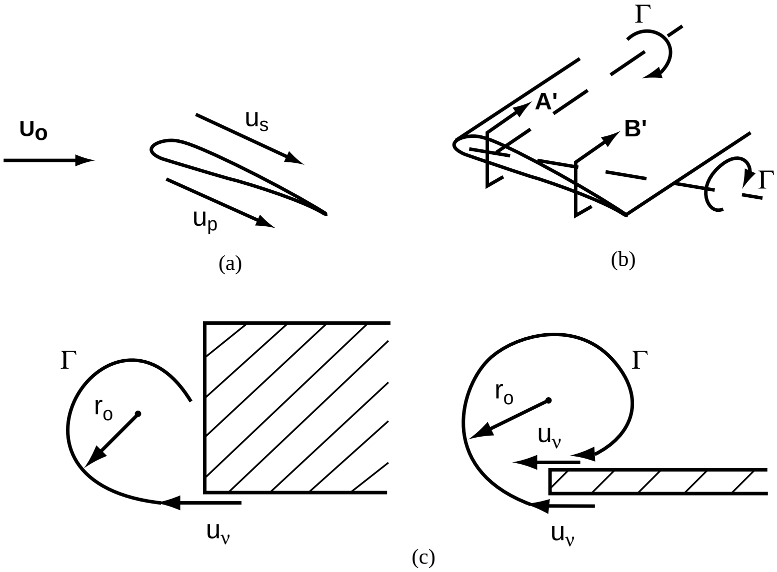

Fig. 9. Illustrations for simplified flap edge velocity calculations: (a) flap inboard section flow, (b) bound and trailed flap vortex circulation, (c) model flap vortex circulation model showing forward section cut A′ and aft section cut B′.

term, [ ], would be unity.) Equating $u_v = u$ at $r = r_0$, we obtain

$$u_v = U_0 C_N c / 8\pi r_0, \tag{3}$$

where the strength Γ is obtained from Eq. (1). Using Eqs. (2) and (3), the velocities on the edge surfaces may be determined. For the pressure side,

$$U_{pr} = \sqrt{(u_{pr})^2_{mean} + u_v^2}, \quad \beta = \tan^{-1}[(u_{pr})_{mean}/u_v]. \tag{4}$$

For the suction side, on the aft section where the vortex crosses to the upper surface, U_{su} is similarly expressed but the subscript *su* replaces *pr*. On the forward section, U_{su}, however, is simply taken as $(u_{su})_{mean}$ and $\beta \approx 90^\circ$. In Table 2, values of these velocities (in terms of Mach number) and angles are given in parentheses to compare with corresponding CFD values for the different sensors. The *pr* and *su* subscripts are dropped. The values were calculated using $r_0 = 0.4\, t_{max}$ and previously mentioned value of $C_N = 1.213$ for $\alpha = 29^\circ$ and $C_N = 1.567$ for $\alpha = 39^\circ$. The maximum flap thickness is $t_{\max} = 0.55$ in. The chosen r_0 appears physically realistic with respect to vortex size and renders velocities and angle values in nominal agreement with the CFD values–but, unlike the CFD values, the velocities and angles have the physically expected (and desirable) flap angle dependence.

Also listed in Table 2 (in parentheses) are calculated approximate values of shear layer or boundary-layer thicknesses δ that one can compare to values that are determined from the CFD flow field previously discussed. The calculated values were determined by equations and extrapolated equations of Ref. [10], as defined below. The boundary-layer thickness at the trailing edge for an untripped symmetric NACA 0012 airfoil at 0° angle of attack is empirically determined to be [10, Eq. (5)]

$$\delta_0 = c \times 10^{[1.6569 - 0.9045 \mathrm{Log} R_c + 0.0596 (\mathrm{Log} R_c)^2]}, \tag{5}$$

where $R_c = cU_0/\nu$ is the Reynolds number based on chordlength c and ν the medium kinematic viscosity. At an angle of attack of α (taken as flap angle here) to the flow, the pressure side thickness δ can be related to δ_0 by

$$\delta/\delta_0 = 10^{-0.0159\alpha}, \tag{6}$$

where α is angle in units of degrees. Note that Eq. (6) is newly determined here based on the data in Fig. 7 of Ref. [10]. It replaces Eq. (8) of Ref. [10] in order to be more valid for large angles. The values of δ, using Eqs. (5) and (6), are 0.0453 and 0.0314 in for 29° and 39° at $M_0 = 0.17$. These are somewhat larger than that listed in Table 2 for the sensors on the pressure and suction sides.

In this paper, δ is used as a normalizing parameter for surface pressure and overall flap noise spectra. Also used in normalizations are δ values for roughened surfaces. This is approximated by the result of an interpolation of δ_0 between the untripped (Eq. (5)) and heavily tripped boundary-layer cases of Ref. [10]. The result is a replacement for Eq. (5) for lightly tripped surfaces,

$$\delta_0 = c \times 10^{[1.787 - 0.9045 \mathrm{Log} R_c + 0.0596 (\mathrm{Log} R_c)^2]}. \tag{7}$$

Another normalizing parameter is an average M_c value at the edge defined as

$$M_{c_{AVG}} = \frac{1}{a_0}\sqrt{U_0^2 + u_v^2}. \tag{8}$$

4. Unsteady surface pressures and analysis

4.1. Surface pressure spectra and acoustic source identification

Fig. 10 presents the unsteady surface pressure spectra (auto-spectrum) G_s for four suction-side edge sensors and two pressure-side sensors (32 and 34) for $M_0 = 0.17$. As previously stated, the data presented in this paper are limited to regions of flat frequency response for the sensors. It is a one-third-octave-band presentation, with the dB levels referenced to p_0^2, where $p_0 = 20\,\mu\text{Pa}$ is the standard acoustic reference. In Fig. 10(a), for $\alpha = 29°$, the levels are shown to be quite variable between sensors with the highest on the suction side at sensors 12 and 16. Referring to Figs. 4 and 7, these two sensors are at opposite sides of the primary flap edge vortex on the suction surface. At $\alpha = 39°$, some relative level changes occur for all sensors. Referring to Table 2, one does not see any obvious correspondence between the velocity definitions over the surface at the sensors and the spectral levels. Fig. 11 presents $M_0 = 0.07$, 0.11, and 0.17 data for two sensors normalized by $q_c^2\delta/U_c$, where $q_c = \rho U_c^2/2$. This type of normalization is common for surface pressure spectra

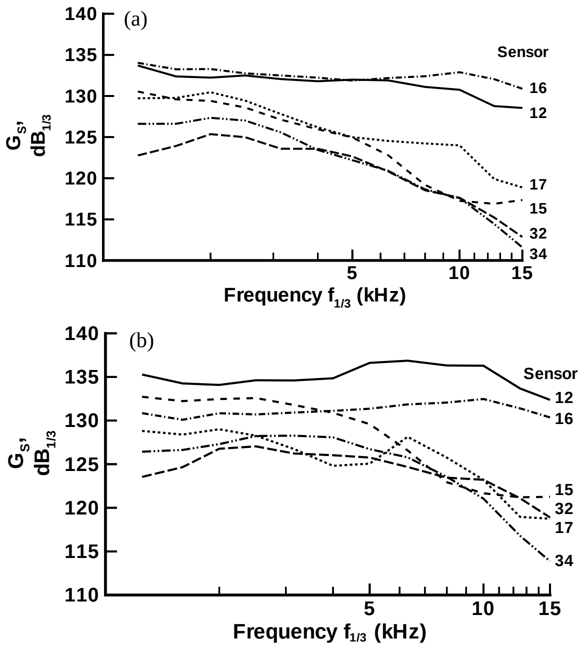

Fig. 10. Surface pressure (one-third octave) spectra for pressure sensors at edge of flap for $M_0 = 0.17$ for different flap angles: (α) (a) 29° and (b) 39°. The suction-side sensors are 12, 15, 16, and 17. The pressure side sensors are 32 and 34.

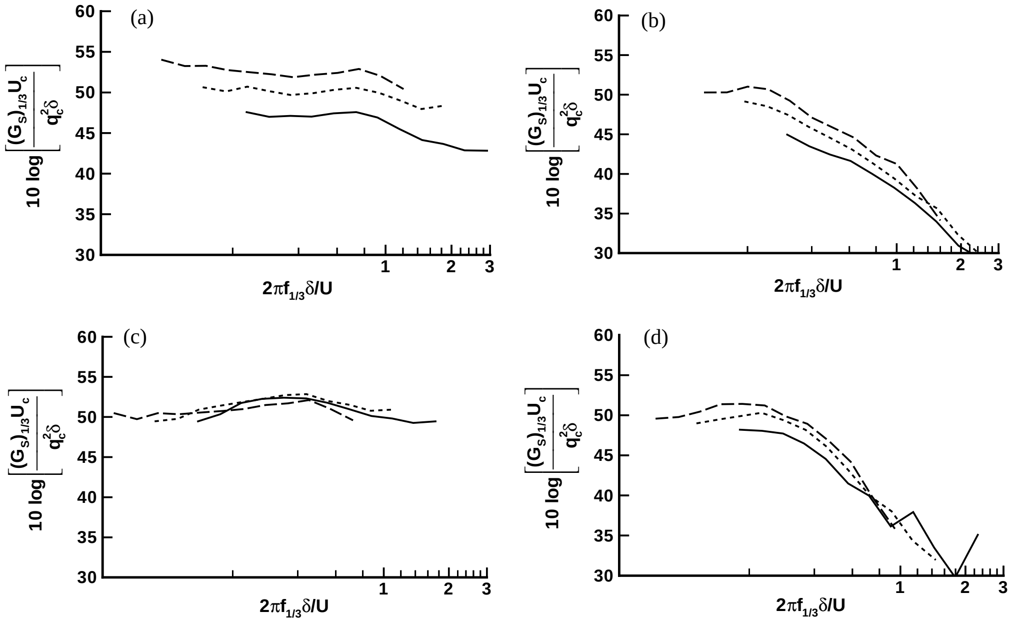

Fig. 11. Normalized pressure (one-third octave) spectra for different angles and flow speeds. For $\alpha = 29°$, the suction side and pressure side sensors are (a) 16 and (b) 34, respectively. For $\alpha = 39°$, the suction side and pressure side sensors are (c) 16 and (d) 34. The key for M_0: ——, 0.07; - - - - -, 0.11; – – – –, 0.17.

under turbulent boundary layers, an example being Ref. [6]. The values for U_c are determined as U_p and U_s from Eq. (4), as was done to obtain values for Table 2. The values for δ are obtained from Eqs. (5) and (6). These values depend on velocity and flap angle, but not chordwise location. It is seen (by the degree of data coalescence) that while tunnel velocity dependence is partially captured, it is not consistent between flap settings. The spectral shapes for each sensor apparently depend greatly on the particular flow phenomena occurring about it–therefore, the local flow phenomena apparently change with angle and velocity variations. The parameter grouping does not capture this. It is noted that the use of the δ and U_c values from Table 2 based on the CFD results produces no improvement in normalization success. It is expected that any such normalizations should be more successful at sensor positions more inboard, away from the edge.

Fig. 12 shows some spectral characteristics that can provide a basis for a noise mechanism hypothesis. The auto-spectra G_s are given for edge and inboard sensors for both the suction and pressure sides. The spectral resolution is $\Delta f = 244$ Hz but the levels are referenced to a $\Delta f = 1$ Hz bandwidth (to put these in a standard power spectral density format). For the suction side, the inboard sensors 21 and 23 are comparable in level to one another and are lower than the edge sensor 16 levels by about 15 dB at 5 kHz. For the pressure side, the levels of the inboard sensors 40 and 42 are comparable, to one another, and are lower than edge sensor 34 by over 15 dB at 5 kHz. The levels for the farther inboard sensor 46 are even lower. This characteristic of increased surface pressure spectral levels, as the edge is approached from inboard is counter to that found for the classical turbulent-boundary-layer (TBL) trailing-edge (TE) noise scatter problem [6]. (There, of course, the radiating edge is the trailing edge rather than the present flap side edge. In that case,

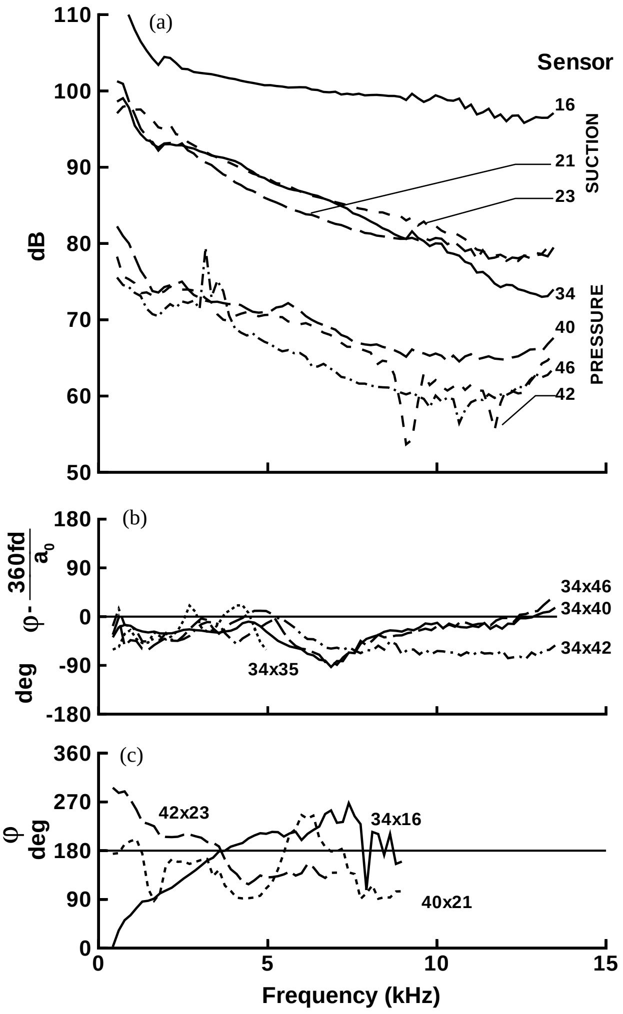

Fig. 12. Surface pressure spectra and phase relationships for edge and inboard sensors. Pressure spectra for (a) suction and pressure sides of flap and cross-spectral phase between (b) pressure side sensors and (c) opposing side sensors. The spectral resolution is $\Delta f = 244\,\text{Hz}$, but levels are referenced to $\Delta f = 1\,\text{Hz}$.

the hydrodynamic (TBL) pressure field is intense upstream of the edge. But very near the edge, the levels decrease, because of pressure scatter (near field noise) that prevents a pressure differential at the edge.) Therefore, the noise level behavior of Fig. 12 suggests a different mechanism than that for the TBL-TE noise problem. This is correspondingly true for the phase behavior to be discussed below.

The hypothesized mechanism for the present flap-edge problem is illustrated in Fig. 13, which shows flow-field influences on unsteady surface pressures. The subject sensors of Fig. 12 are shown mounted in a "section cut", the edge sensors are located at y_A and the others are at y_B and y_c of Fig. 4. The edge 16 and 34 sensors are not aligned chordwise. The conceptual illustration is

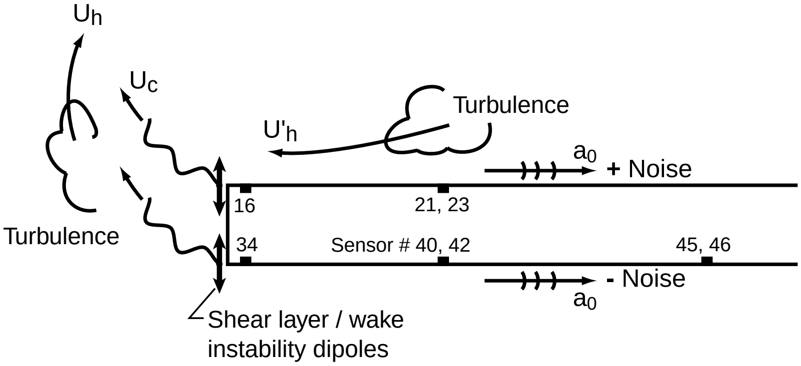

Fig. 13. Hypothesized flow and acoustic features affecting unsteady surface pressures at sensors.

consistent with the shear layer instability models [26,30,33] for noise production. Shear layer instabilities are shown being shed at velocity U_c at the edges near sensors 16 and 34. The velocities U_c, U_h, and U_h' should be of the same order of magnitude to that of velocity u_v of Fig. 9(c). The flow is relatively smooth on the pressure side but becomes turbulent as it moves (convecting at velocity U_h) around the edge towards the suction side. The suction side turbulence is within the fringes of the primary vortex and convects at velocity U_h' above the surface. Fig. 13 represents the shear layer instability noise source as dipoles (that are distributed chordwise). A portion of the noise that is radiated travels along the surface in the spanwise direction at the speed of sound a_0. Both dipoles radiate to both sides with opposite signs (180° out of phase). Of course, Fig. 13 is a sectional presentation. In reality, there are a number of independent dipoles radiating at different sections–the effective number of which depend on disturbance correlation scales.

The observation that the noise levels of Fig. 12 are diminished as distance from the edge is increased is consistent with the model of Fig. 13. The phase behavior is also consistent as is now shown. The phase φ between sensor 34 and the inboard sensors, on the same pressure side, is normalized by subtracting (fd/a_0) 360, where f is the frequency and d is the distance from 34 to the other sensors (that one determines from Table 1). A result of 0° would show that the correlated components of the respective sensors are the same signals that are simply time delayed at the speed of sound. The results shown in Fig. 12 show this to be generally true, except for a $45 \pm 15°$ offset. However, note that in Ref. [6], the scatter term for TE noise was found to have a 45° offset in scatter-pressure phase (in addition to that due to time delay) between the edge near field and a point away from the edge. Hence, this is consistent with Ref. [6]. Additional confirmation of the conceptual model is provided in Fig. 12 by the phase of sensors on opposite sides of the flap. The phases are not normalized. It is seen that for sensors away from the edge, there is roughly a 180° shift over much of frequency range. At the edge sensors 16 and 34, an approximately 180° phase is attained near 4 kHz. At lower frequencies, the phase is dominated by hydrodynamic convective effects, symbolized in Fig. 13 by turbulence moving at U_h. The linear phase slope, starting near zero frequency, suggest that U_h between the sensors is about 0.22 times a_0. Similar values were found for U_h' using the sensors on the suction-side surface. This compares favorably with computed (CFD and simplified) convective velocities. It was found that hydrodynamic-convection effects generally dominate the phase relations between most edge

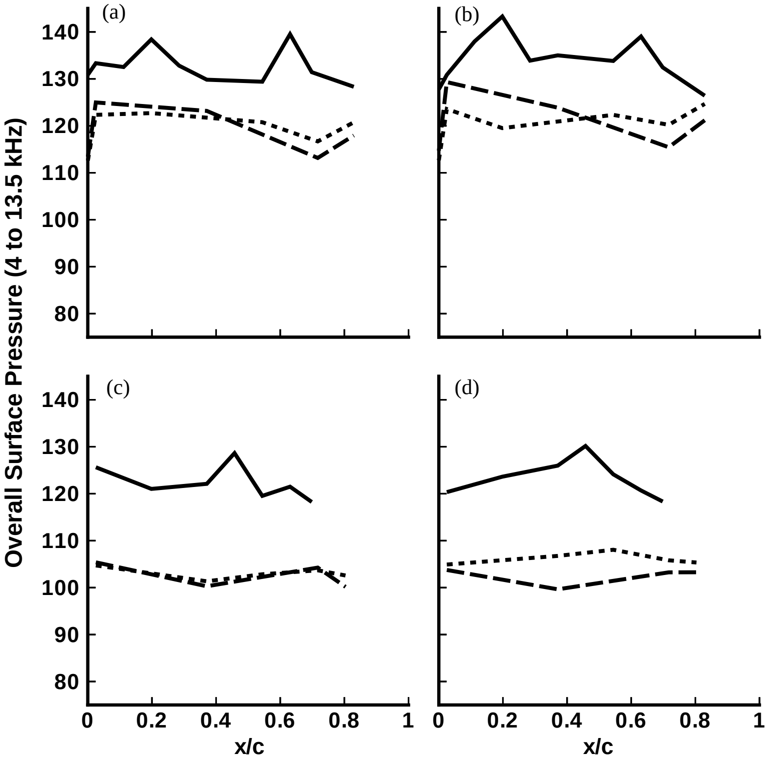

Fig. 14. Chordwise distribution over FLAT edge flap region of band-limited overall surface pressure levels. $M_0 = 0.17$. For the suction side (a) $\alpha = 29°$ and (b) $\alpha = 39°$. For the pressure side (c) $\alpha = 29°$ and (d) $\alpha = 39°$. Referring to spanwise cuts of Fig. 4 and Table 1, the keys are as follows: ——, edge A; - - - -, inboard B; – – –, inboard C.

sensors, as well as those over the suction surface. Most of these effects are not directly related to noise production. However, this does not mean that the individual sensor auto-spectrum is not dominated by noise-related effects–it just means that the hydrodynamic effects are larger scale and thus correlate better over distance. The present edge sensors are deemed too far apart for cross-spectra to determine pertinent noise source information, such as scale lengths.

Fig. 14 serves to summarize key features of the surface pressures. The Fig. presents chordwise distributions of integrated surface pressure levels for sensors, at sections A, B, and C of Fig. 4, for both pressure and suction sides of the flat edge flap for $\alpha = 29°$ and 39°. The levels result from integrating the spectra from 4.0 to 13.5 kHz. The low-frequency limit of 4.0 kHz was chosen in order to de-emphasize purely hydrodynamic effects (see discussion above). For both flap angles, the levels at the suction-side edge A appear peaked in the general locations of the chordwise extremities of the vortex on the suction side. On the pressure side, one peak is observed near the flap mid-chord. The inboard sections B and C have levels that are relatively uniform over the chord and substantially lower than the edge levels. Section C levels are generally lower than those of section B. This is consistent with the noise mechanism modelling depicted in Fig. 13. The higher levels on the suction side for the inboard

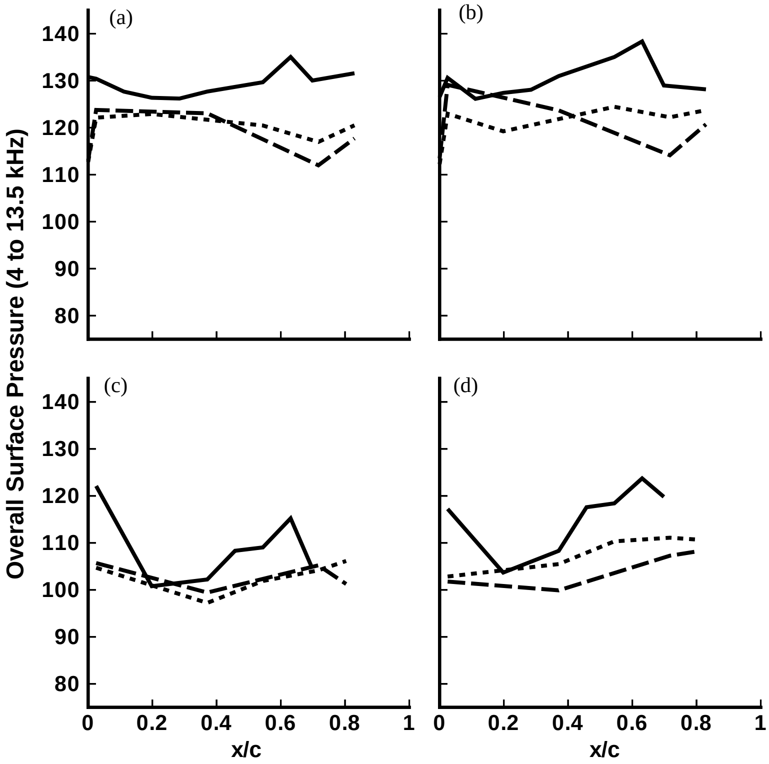

Fig. 15. Chordwise distribution over ROUND edge flap region of band-limited overall surface pressure levels. Key as per Fig. 14.

sensors, with respect to the edge levels, are expected to be due to the presence of strong turbulence on the suction side.

Fig. 15 presents chordwise level distributions for the round edge flap sketched in Fig. 2. The character of the distributions is somewhat similar to that of the flat edge, but section A sensor levels are reduced to nearly that of the inboard sensor levels. This is because they are further inboard of the edge than was case for those on the flat edge flap. The noise mechanism details that are depicted in Fig. 13 are not directly applicable to this round edge flap case. However, flow shear/boundary-layer instabilities still should be the basic mechanism, but with a different scattering geometry and correlated fluctuation length scales.

4.2. Coherent output power analysis

The surface pressure levels in Figs. 14 and 15 do not necessarily indicate the local noise-source strength distribution. The inboard levels contain substantial contributions from hydrodynamic convection effects and noise radiating along the surface–not sources of noise. (Note that strictly speaking, in terms of the Ffowcs Williams and Hawkings equation [43], the inboard pressures are by definition part of the noise region that should be accounted for. This is discussed in the next section.) The edge sensors for the flat edge flap, however, are in the near field of the source and can represent the source, except to the extent that it is affected by non-radiating fluctuating pressure components. This section is concerned with providing some measure of the noise source distribution along the flap edge.

The coherent output power spectrum [44] is defined as

$$COP_s = \frac{|G_{a,s}|^2}{G_a} = \gamma^2_{a,s} G_s, \tag{9}$$

where, for present purposes, this is the spectrum of the surface pressure sensor (subscript s) output that is coherent with the SADA array (subscript a) output when steered to this surface sensor(s) on the flap. The auto-spectra are G_a and G_s. The cross-spectrum between signals is $G_{a,s}$ and the coherence is $\gamma^2_{a,s}$. The phase associated with COP_s is the cross-spectral phase $\varphi_{a,s}$. In the present data processing, a data-block time-shifting procedure is used to avoid serious bias and statistical errors, as well as to put the data in a useful phase format. The microphone raw time data are time shifted (offset) by an amount close to the value of $\tau_{a,s}$, which is the time required for noise to be transmitted from the sensor to the array. The array processing shear layer refraction correction code determines $\tau_{a,s}$. (The $\tau_{a,s}$ values were evaluated to be accurate within less than the time it takes to acoustically travel 0.25 in.) Final adjustment to obtain the full $\tau_{a,s}$ shift effect, for each

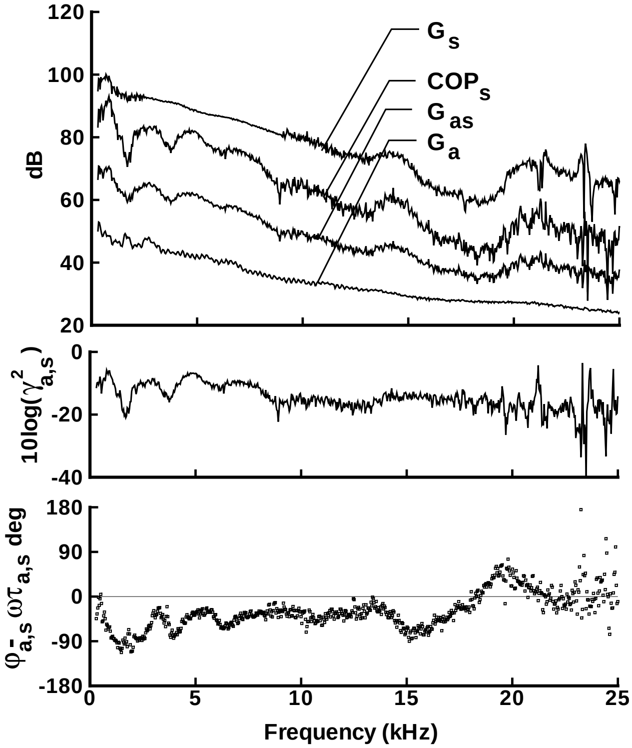

Fig. 16. Coherent output power spectral processing results, for the flat edge flap, relating the sensor 34 pressure measurement and the SADA noise measurement for $M_0 = 0.17$ and $\alpha = 39°$. The spectral resolution is $\Delta f = 34.88$ Hz, but levels are referenced to $\Delta f = 1$ Hz.

individual microphone and sensor, is done in the frequency domain. With regard to the cross-spectrum, this effectively puts the source region in “retarded” coordinates, where the phase related to noise transmission time is removed, that is

$$(G_{a,s})_{\tau_{a,s}} = G_{a,s}\mathrm{e}^{-\mathrm{j}\omega\tau_{a,s}}, \quad (\varphi_{a,s})_{\tau_{a,s}} = \varphi_{a,s} - \omega\tau_{a,s}, \tag{10}$$

where the radian frequency $\omega = 2\pi f$.

Fig. 16 shows results of COP processing for sensor 34 (pressure side) with respect to the output of the SADA when steered to the sensor for the test case listed. The SADA is positioned at $\phi = 107^\circ$. The two auto-spectra, the cross-spectrum, and the COP_s spectra are shown. (Note that the differences in surface pressure auto-spectrum smoothness are related only to an application of a calibration transfer function. As previously mentioned, the surface pressure data should be accurate below about 13.5 kHz.) The difference in levels between G_s and COP_s is $10\,\mathrm{Log}(\gamma^2_{a,s})$, which is shown in the figure. As is shown in the next section, if a surface element (represented here by sensor 34) is a direct radiator to the noise field, one would expect the phase $(\varphi_{a,s})_{\tau_{a,s}}$ to equal a

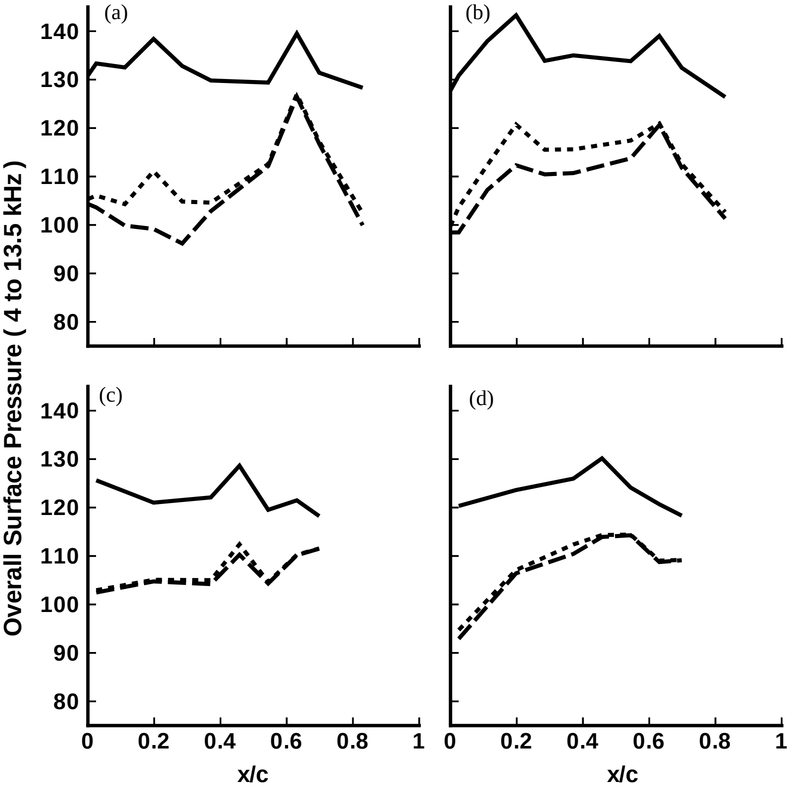

Fig. 17. Chordwise distribution over FLAT edge flap of band-limited overall surface pressure levels and related COP levels. $M_0 = 0.17$. For the suction side (a) $\alpha = 29^\circ$ and (b) $\alpha = 39^\circ$. For the pressure side (c) $\alpha = 29^\circ$ and (d) $\alpha = 39^\circ$. The keys for dB levels are as follows: ——, overall; - - - -, COPS with phase suppressed; – – –, COPS with phase not suppressed.

constant $-90°$. The phase is shown in Fig. 16 to be generally constant, but at a phase value on the order of $-40°$ or $-50°$. However, this is consistent with a $45°$ offset expected for an edge in a scatter field as mentioned in the last section. This phase behavior will be again discussed.

Fig. 17 presents chordwise distributions of integrated surface-pressure COP levels for the edge sensors (along section A). For comparison, the auto-spectra distribution from Fig. 14, for the same integration frequency range, is shown. No data from inboard sensors are shown because these are assumed not to be in the noise source region. The COP distributions represent more realistic distributions of noise-source strength distribution than does the auto-spectra. The COP results eliminate that portion of surface pressure that is not related to the noise field. So non-radiating hydrodynamic fluctuation contributions are removed, which lowers the COP levels with respect to the auto-spectra levels. Also, however, there is an additional cause of the lower levels for the COP results. The correlation area that each sensor represents is small and there are a large number of correlation areas over the flap edge that contribute to the total noise. For example, if there were uniform noise-source strength (say with no non-radiating hydrodynamic fluctuations present) and the COP were uniformly 20 dB lower than the auto-spectra, one could hypothesize that there are "effectively" 100 independently radiating noise-source areas across the flap edge. Fig. 17 shows two COP distributions. One is where phase is not considered in the integration

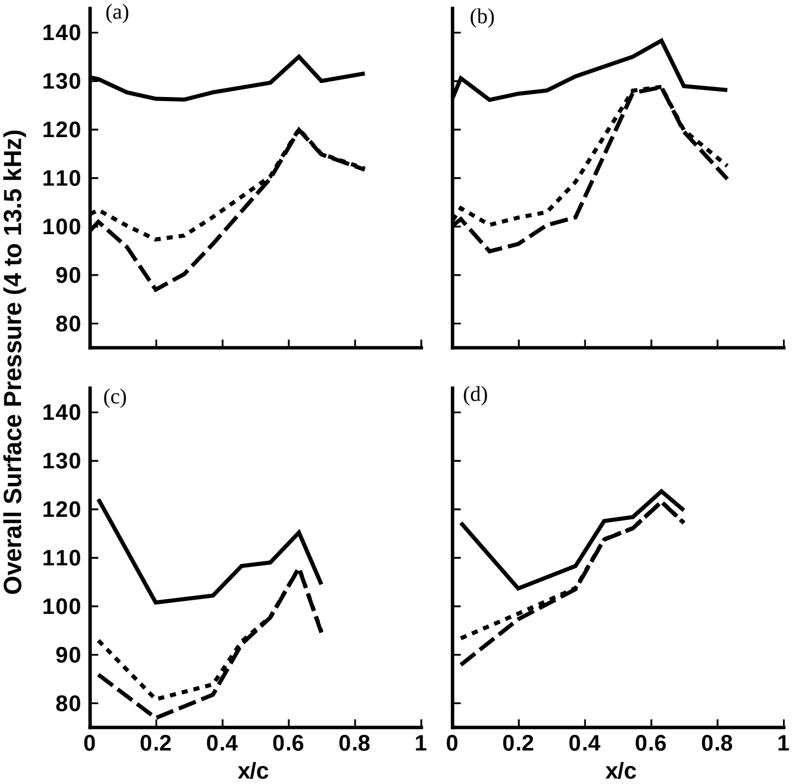

Fig. 18. Chordwise distribution over ROUND edge flap of band-limited overall surface pressure levels and related COP levels. Key as per Fig. 17.

(straight pressure-squared-type summing) of the frequency bands. The other distribution is where the phase is used in the integration (vectorial-type summing). The latter is lower in level and is the preferred presentation because those portions of hydrodynamic and/or acoustic fluctuations, which are related to noise production only in an indirect way, are substantially eliminated. Consider the COP peak near 20% chord for the phase-suppressed distribution on the suction side for $\alpha = 39^\circ$. Phase data (not shown), indicate that the fluctuations which cause the high COP levels were related to turbulence and/or noise, that are in turn correlated with noise production at another portion of the edge. Since the phase $(\varphi_{a,s})_{\tau_{a,s}}$ has to be constant for that portion of COP related to the direct radiation from the sensor to the microphones, the summing of COP bands vectorially can substantially remove (bias against) the "indirect" contributions to COP. This should make the COP more representative of the actual source distribution. The COP distributions in Fig. 17 show that, for both of the flap angles, the noise is most strongly radiated near 65% chord on the suction side and near 50% on the pressure side of the flap edge.

Fig. 18 shows COP results for the round flap edge, in the format of Fig. 17. The same comments apply here, as for the flat edge flap, except that the edge sensors may be not be fully in the source region, as mentioned for the auto-spectra integrated level plots of Fig. 15. Still, one can make the statement that the chordwise noise source appears clearly and strongly located near 60% chord for both pressure and suction sides for both flap angles.

5. Noise predictions based on surface pressure spectra

5.1. Causality spectra prediction

A causality spectral approach is developed in this section that helps establish the relative and quantitative importance of the noise-source regions of the flap. Previous success has been found by Siddon [45], using cross-correlation methods and the acoustic relationships of Curle [46], in determining surface noise-source distributions. This causality approach employed cross-correlations between surface pressure sensors and microphones. For several simple and small surface shape cases under Siddon's study, the method provided a physical characterization of the noise source. However, when the sources were non-compact, acoustically or aerodynamically, the phase variations greatly hindered correlation function interpretation and their usefulness. In this paper, we revisit the causality idea using spectral methods and for the first time validate a causality prediction with measurement for a distributed source.

The noise field is given by the Ffowcs Williams and Hawkings equation [43] (a form similar to Curle's equation but generalized for arbitrary fluid and surface motion). For low-Mach number flows and for surfaces with steady (or no) motion with respect to the observer, distributed volume quadrupole and surface monopole source components in the equation are negligible. Assuming surface shear stresses are small compared to local surface pressures, the following equation form can be found, relating the acoustic pressure $p_a(\mathbf{x}, t)$ at location $\mathbf{x}$ and time t to the surface pressure $p_s(\mathbf{y}, \tau)$ at position $\mathbf{y}$ and retarded time τ:

$$p_a(\mathbf{x}, t) = \frac{1}{4\pi a_0 r} \int_{S(\mathbf{y})} \frac{\mathbf{n} \cdot \mathbf{r}/r}{(1 - \mathbf{M_0} \cdot \mathbf{r}/r)^2} \left[\frac{\partial p_s(\mathbf{y}, \tau)}{\partial \tau} \right] \mathrm{d}S(\mathbf{y}). \tag{11}$$

Fig. 19 shows the geometry of the flap in the open-jet tunnel flow of Mach number $\mathbf{M_0} = \mathbf{U_0}/a_0$, where $\mathbf{U_0}$ is the tunnel test section velocity. The elemental surface area $\mathrm{d}S(\mathbf{y})$, at $\mathbf{y}$ with normal $\mathbf{n}$, is seen with respect to a ray path of length $r = |\mathbf{r}|$, where $\mathbf{r} = \mathbf{x} - \mathbf{y}$. Shear layer corrections performed in the array processing code corrects the results at the actual SADA out-of-flow position to an 'effective' observer position $\mathbf{x}$ in an extended flow field without a shear layer. The medium speed of sound is denoted by a_0. The retarded time is defined implicitly by

$$\tau = t - |\mathbf{r} - \mathbf{U_0}\tau|/a_0, \tag{12}$$

as pointed out by Guo [33]. In the far-field limit for $\mathbf{x}$,

$$p_a(\mathbf{x}, t) = \frac{1}{4\pi a_0 r D^2} \int_{S(\mathbf{y})} \cos\theta \left[\frac{\partial p_s(\mathbf{y}, \tau)}{\partial \tau}\right] \mathrm{d}S(\mathbf{y}), \tag{13}$$

where $D = 1 - \mathbf{M_0} \cdot \mathbf{r}/r \approx 1 - \mathbf{M_0} \cdot \mathbf{x}/|\mathbf{x}|$ and $\cos\theta = \mathbf{n} \cdot \mathbf{r}/r$. The retarded time becomes

$$\tau \approx \left(t - \frac{r'}{a_0}\right), \tag{14}$$

where $r' \approx rD^2$, which is shown in Fig. 19. The distance r', which is used in the shear layer processing code [35] of this study, is that between the effective observer position and source position in an ideal quiescent acoustic field. In this co-ordinate system, $\cos\theta$ is replaced by $\cos\theta' = \mathbf{n} \cdot \mathbf{r'}/r'$. Upon defining the Fourier transform

$$\Im[p_s(\mathbf{y}, \tau)] = \int_{-\infty}^{\infty} p_s(\mathbf{y}, \tau)\mathrm{e}^{-\mathrm{j}\omega t}\,\mathrm{d}t = P_s(\mathbf{y}, \omega), \tag{15}$$

$$\Im[\frac{\partial}{\partial \tau} p_s(\mathbf{y}, t - r'/a_0)] = -\mathrm{j}\omega P_s(\mathbf{y}, \omega)\mathrm{e}^{-\mathrm{j}\omega r'/a_0}, \tag{16}$$

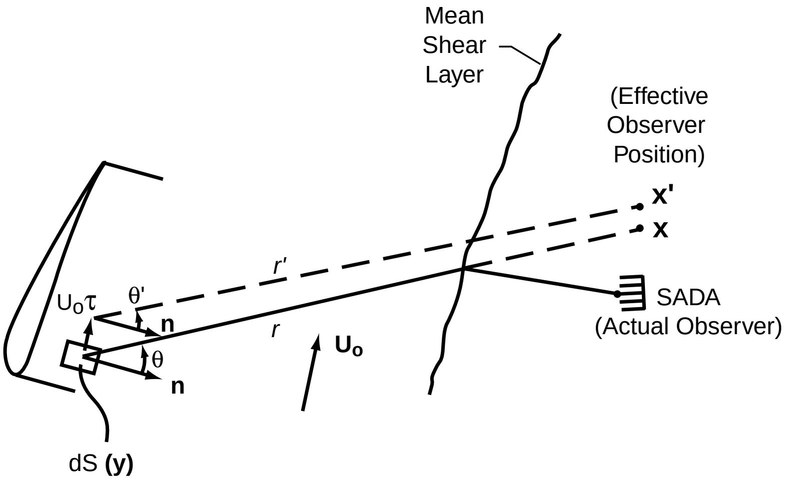

Fig. 19. Flap surface geometry with respect to ray path to noise observer.

the Fourier transform of the acoustic field is

$$P_a(\mathbf{x},\omega) = \frac{-\mathrm{j}\omega}{4\pi a_0 r'} \int_{S(\mathbf{y})} \cos\theta' P_s(\mathbf{y},\omega) e^{-\mathrm{j}kr'}\, \mathrm{d}S(\mathbf{y}), \tag{17}$$

where $k = \omega/a_0$. Multiplying both sides of Eq. (17) by the complex conjugate of $P_a(\mathbf{x},\omega)$ and taking the ensemble average, we get the auto-spectrum of the noise field

$$G_a = \langle P_a^*(\mathbf{x},\omega) P_a(\mathbf{x},\omega) \rangle = \frac{-\mathrm{j}\omega}{4\pi a_0 r'} \int_{S(\mathbf{y})} \cos\theta' \langle P_a^*(\mathbf{x},\omega) P_s(\mathbf{y},\omega) \rangle \mathrm{e}^{-\mathrm{j}kr'}\, \mathrm{d}S(\mathbf{y}). \tag{18}$$

Now upon evaluating this with respect to elementary surface areas $\Delta S(\mathbf{y})$, the following results:

$$G_a = \langle P_a^* P_a \rangle = \frac{-\mathrm{j}\omega}{4\pi a_0 r'} \sum_{\Delta S(\mathbf{y})} \cos\theta' \langle P_a^* P_s \rangle \mathrm{e}^{-\mathrm{j}kr'} \Delta S(\mathbf{y}). \tag{19}$$

The components, making up the sum in the right-hand of Eq. (19), are defined here as the causality spectra associated with the surface area elements $\Delta S(\mathbf{y})$ and represent their contribution to the total noise G_a. The auto-spectrum G_a must be a positive real quantity, while the components are complex quantities. Eq. (19) is valid under the present assumptions, in particular that only surface dipole noise sources are important, and that the sum is taken over infinitesimal $\Delta S(\mathbf{y})$ areas over all of $S(\mathbf{y})$. Eq. (19) includes all the hydrodynamic pressure fluctuations (correlated or not between different $\Delta S(\mathbf{y})$ areas), as well as related pressure scatter (near-field noise). It is important to note that non-radiating turbulence hydrodynamic effects, with their various complex phase contributions, may greatly dominate the individual terms. The full evaluation of the sums are needed to completely self-cancel the non-radiating contributions. Such concerns not only apply to Eq. (19) but also to the Ffowcs Williams and Hawkings equation in general.

In those practical application cases where $\Delta S(\mathbf{y})$ must be finite in size and limited in number, the validity of Eq. (19) requires that $\Delta S(\mathbf{y})$ be chosen and interpreted carefully. As previously noted in discussions pertaining to Fig. 17, many of the pressure sensors of the present problem (particularly the inboard sensors) were found to be indeed dominated by non-noise producing hydrodynamic and acoustic effects, for which portions are correlated with the noise. The use of only the edge sensors of the flat edge flap should reduce extraneous ‘noise’ in any prediction and data comparison. The model then reduces to a line of dipoles along each side edge, with the presence of the inboard flap surfaces not included in the solution for the acoustic radiation. To account for the “half-baffle” acoustic effect of the inboard surfaces, the solution can be multiplied by a factor of two (2). This is taken to give an accurate presentation for small θ'.

For the present study, Eq. (19) is evaluated using data from the flat edge flap. Our attention is restricted to the edge sensors 1–18 and 30–36 as representing the source region. The following relation is evaluated:

$$G_a = \sum_i \langle P_a^* P_a \rangle_i = \frac{2\omega}{4\pi a_0} \sum_i \left[\frac{\cos\theta' \mathrm{e}^{-\mathrm{j}\pi/2}}{r'} \right] \langle (P_a \mathrm{e}^{\mathrm{j}kr'})^* P_s \rangle L\ell_1, \tag{20}$$

where the additional factor of 2 included is discussed above. The cross-spectral term containing the retarded time shift is identified as $(G_{a,s})_{\tau_{a,s}}$ of Eq. (10). The area $\Delta S(\mathbf{y})$ has been replaced by $L\ell_1$. We take L to be the sum of correlation length scales that sensor i represent and, nominally,

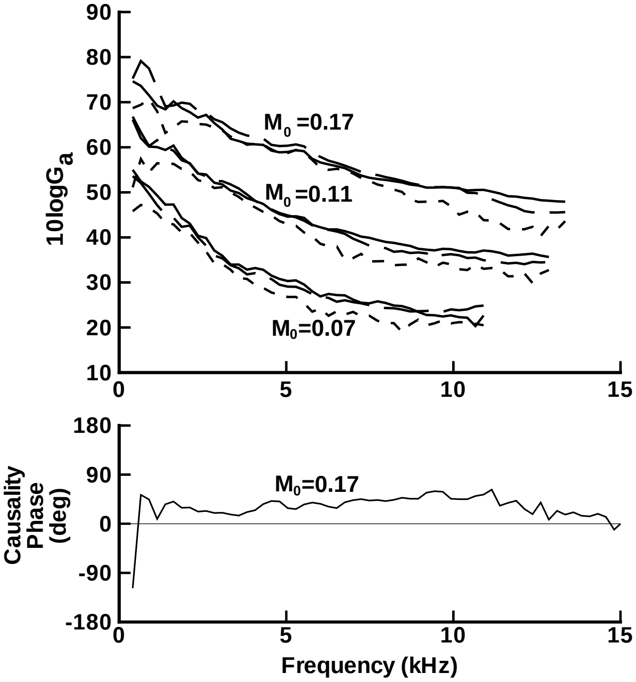

Fig. 20. Causality noise prediction comparisons for flat edge at different tunnel speeds for $\alpha = 29°$. $\eta = 0.3$, $\Delta f = 244$ Hz. The keys for spectra are as follows: ——, measured; - - - -, causality prediction; – – –, causality prediction (phase suppressed). The key for causality phase is: ——, measured.

the sum of all L equals the edge circumference. The correlation length scale ℓ_1 in the flap longitudinal direction (spanwise direction in Fig. 4) is taken as $U_c/\eta\omega$. This relationship for scale length is often used in turbulent boundary-layer (TBL) pressure scaling. In the present study, the available data provided no satisfactory means to determine values of η. In Ref. [6], η values for a TBL was found to be 0.14 and 0.19 for the cases examined. For the following predictions, we use the value $\eta = 0.3$. This choice is discussed in a following section.

Causality predictions and comparisons with measured noise is presented in Fig. 20 for the flat edge flap at $M_0 = 0.07$, 0.11, and 0.17 with $\alpha = 29°$. The SADA is positioned at 107°. Two causality prediction results are shown. The predictions based on Eq. (20) are the prediction curves showing the lower levels. The associated phase for the $M_0 = 0.17$ speed case is shown plotted below the spectra. Ideally, the phase of G_a should be zero. However, the phase is seen to be approximately 30–50°. This is consistent with the aforementioned 45° phase shift in the edge sensor pressures located in the near field of the edge scatter. If G_a were fully evaluated over the whole surface (not possible with limited data) then the phase would be expected to be near zero. The other causality prediction results shown are where the phases in Eq. (20) are suppressed for each individual contribution. Forcing phase to be zero removes additive random phase error in the cross-spectra and errors related to time delay variability for each sensor. It may, however, add bias error of an unknown amount by adding correlated components, when they would otherwise properly cancel. Still the results appear to compare well over the whole spectra range. For the

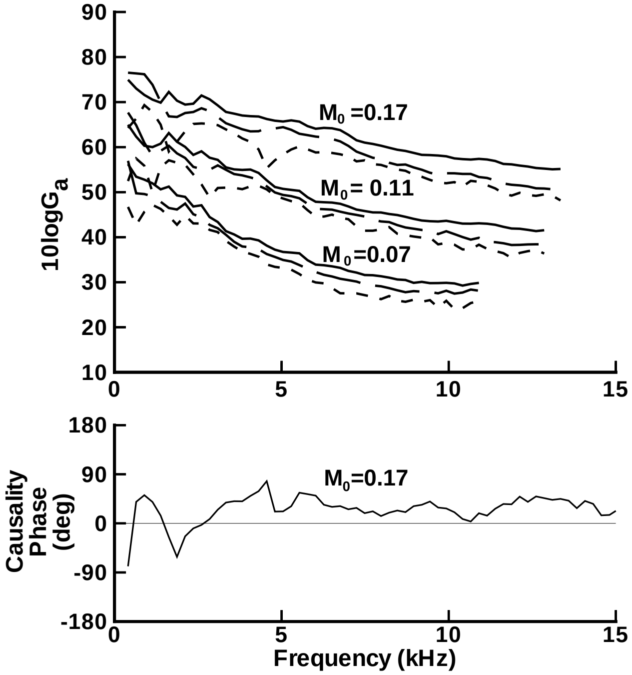

Fig. 21. Causality noise prediction comparisons for flat edge at different tunnel speeds for $\alpha = 39°$. Key as per Fig. 20.

$\alpha = 39°$ case, the same prediction comparisons are made. This is shown in Fig. 21 in the same format as Fig. 20. For this case, the predicted levels are lower than measured levels, particularly for the causality predictions where phase is included. Note correspondingly that substantially larger phase variations are seen compared to those in Fig. 20. This indicates that these predictions based on only the edge sensors are less representative of the total noise production. The influence of the burst vortex, associated with this $\alpha = 39°$ flap angle case, may cause the noise source region to be more distributed over the surface.

5.2. Scatter edge noise prediction

Brooks and Hodgson [6] used the trailing edge noise theory of Howe [47] and measured surface pressures to predict trailing edge noise due to the passage at the edge of turbulent boundary-layer flow. The present edge noise problem is that of shear layer wake instability and resultant shedding of unsteady vorticity from the edges. Howe's theory was developed primarily with the former case in mind. However, the solutions should be generally valid here as long as one restricts attention to pressures in the immediate vicinity of the edge and that certain parameters can be properly defined. Fig. 8 is used to illustrate several parameter choices in doing this. For the velocity field $\mathbf{U}(z)$ above an edge sensor, a local maximum of magnitude U_c is reached at a height δ. These values correspond to those listed in Table 2, along with corresponding skew angle β_c. One hydrodynamic wavenumber component of the instability wake sheet is shown in Fig. 8 as being shed from the edge region. It is assumed that this sheet perturbation (shown as a corrugation) convects at this same speed U_c and angle β_c after it leaves the surface. The analysis also assumes that the edge sensor is in the very near field of the edge shedding and that the local edge thickness is much smaller than the related acoustic wavelength.

Eq. (72) from Howe [47] (Eq. (32) from Ref. [6]) gives the noise spectrum G_a at a location in the far field due to the trailing edge (TE) noise from a thin plate of length L, in terms of the TE pressure field. This is, in the present terminology,

$$G_a = \frac{2}{\pi r^2}\left(\frac{U_c L}{a_0}\right)\frac{|\cos\theta|\sin^2(\vartheta/2)\cos\beta_c}{(1+M_{or})^2(1-M_{U_c r})^2(1-M_{U_1}|\cos\theta|)}\cdot\int_{-\infty}^{\infty}\Pi_{te}(\mu_1,\omega\sin\theta/a_0,\omega)\,\mathrm{d}\mu_1, \qquad (21)$$

where θ is the observer angle defined in Fig. 19. The observer azimuth angle ϑ is measured from the negative of the y−axis shown in Fig. 4 (ϑ equals 180° along the spanwise surface and equals 90° normal to and above the flap surface). The Mach number terms are $M_{0r} = U_0\sin\theta/a_0$, $M_{U_c r} = U_c\cos\vartheta/a_0$, and $M_{U1} = U_c\cos\beta_c/a_0$. Eq. (21) ignores one of the Mach number terms of Ref. [47], see Ref. [6]. The integral is taken over a pressure wavenumber spectrum function Π_{te} with respect to the wavenumber μ_1 for the direction normal to the edge. In evaluating the integral, we use the definition of Π_{te} from Ref. [6] (Ref. [47] uses an alternate but consistent definition), to obtain

$$\int_{-\infty}^{\infty}\Pi_{te}\,\mathrm{d}\mu_1 = (G_s)_{te}\ell_3/\pi, \qquad (22)$$

where $(G_s)_{te}$ is the surface pressure spectrum at the edge and ℓ_3 is the correlation length scale in the lateral (edgewise along chord) direction. The assumed form of ℓ_3 is

$$\ell_3(\omega) = \frac{U_c\cos\beta_c}{\varsigma\omega}. \qquad (23)$$

The noise is predicted as a sum of contributions from individual edge lengths each represented by an edge sensor. Similar to Eq. (20) for the causality prediction, the total noise is

$$G_a = \sum_i [G_a]_i, \qquad (24)$$

where each $[G_a]_i$ is determined using Eqs. (21)–(23). As mentioned for the longitudinal scale factor ℓ_1 in the last section, correlation scales for the present mechanism were not determinable from the present data. In the following predictions the value of $\varsigma = 2.0$ is chosen compared to a value of 0.6 (measured for the problem of a TBL pressure field) used in Ref. [6]. This choice and other assumptions are discussed in the next section.

The predictions are compared to measured noise for the two flap angles at different tunnel speeds in Fig. 22. The measured noise spectra are the same as presented in Figs. 20 and 21. The chosen value of ς results in good agreement for the 29° flap angle, as well as the low-speed conditions for the flap angle of 39°. The higher speeds for 39° show predictions to be lower than measured. This general trend, of course, was also found for the causality prediction comparisons using the same sensors. One can then suggest that for the 39° flap case, where the vortex is known to burst, the edge sensors may not fully represent the noise production region.

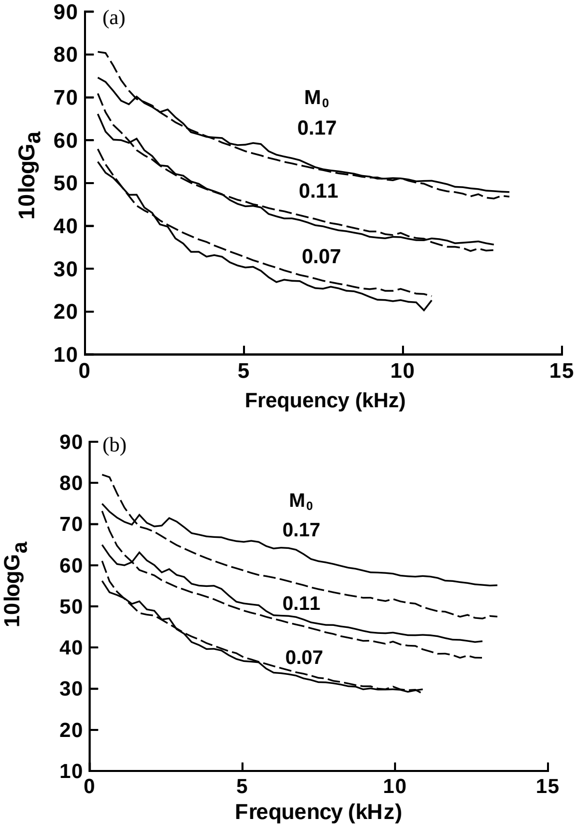

Fig. 22. Scatter-theory noise prediction comparisons for flat edge flap at different tunnel speeds. $\varsigma = 2.0$. $\Delta f = 244$ Hz. The two flap angles are (a) $\alpha = 29°$ and (b) $\alpha = 39°$. The spectra key is: ——, measured; - - - -, prediction.

5.3. Discussion of prediction results

The present predictions strongly support the basic noise mechanism model of Fig. 13 for the flat edge flap. The good prediction results show that the edge sensors can properly represent the noise-source region. However, the prediction and data comparisons suggest this may not be fully true for the vortex bursting case, where the noise is under-predicted. It is likely that the source is just more distributed over the surface. (At the low speeds of the present test, it is unlikely that any volume noise-source terms contribute significantly–even with vortex breakdown.) The two predictions are different in their input requirements. The causality prediction and the COP analysis can be regarded as being related, because of their dependence on cross-spectral processing between the noise and the surface pressure sensors. Note that the causality predictions require little flow information input, with velocity entering only through the definition of correlation length. The causality prediction is primarily one of a noise-correlated force distribution definition, modelled here as a line-dipole taking the surface into account acoustically only through the multiplicative factor of two. The scatter edge noise prediction is more of a "full" prediction, which includes source directivity in the solution. It requires more flow information than the causality prediction. However, for both predictions, the lack of knowledge about pertinent correlation scale lengths required assumptions. The values for decay factors η and ς were chosen to render good overall quantitative comparisons. These correspond to scale lengths of $\ell_1 \approx 0.4$ in and $\ell_3 \approx 0.06$ in at 5 kHz. The ratio $\ell_1/\ell_3 \approx 7$ is compared to a value of about 4 for the different scatter noise problem (TBL-TE) of Ref. [6]. Still, the ratio $\ell_3/\delta \approx 1.5$ appears to be "reasonable" for the present mechanism, although $\ell_1/\delta \approx 10$ may not be. Subsequent investigations should reexamine the correlation scale issue, particularly key parameters such as the disturbance velocity magnitude U_c and skew angle β_c. With regard to noise directivity, it is noted that no assessment has been made here. Measurement presentations, to follow, show that the directivity as implied by the $\sin^2(\vartheta/2)$ term of Eq. (21) does not generally hold. As will be discussed, this is believed due to the finite dimensions of the present flap edge compared to the acoustic wavelength–in contrast to the thin edge assumption of the analysis.

6. Noise directivity and spectra scaling

6.1. Noise-source distribution from array scanning

Acoustic results from the array are shown in Fig. 23 for the flat and round flap edges. The results are obtained from the SADA by electronically scanning a plane projected through the airfoil main element chordline. The position of the SADA corresponds to the model being in an "over-flight" position. An outline of the main element is shown with the leading edge at 24 in and trailing edge at almost 40 in in tunnel coordinates. The flap is on the right and the edge is seen centered in the picture. The dB levels shown are the outputs of SADA when it is steered to the scanning locations. The contour levels are highest at the flap-edge location. These levels at the flap edge have been shown [36] to be the levels that a single microphone would measure for the noise emitted from the flap edge. The rapid roll-off in levels away from the flap edge shows the sharpness of the array in rejecting unwanted extraneous noise from regions other than the edge. The contours shown are for 12.5 kHz one-third octave levels. Because of the microphone shading algorithm methodology [35,36], other frequencies from 10 to 40 kHz show similar spatially invariant patterns. At lower frequencies, the resolution decreases (patterns widen) and the array rejection of extraneous noise is reduced. Still the levels from the vicinity of the flap edge should have little contamination for frequencies above approximately 3 kHz. The spectral output of the SADA should hence represent only that noise which is radiated from the flap-edge region. Noise directivity (shown in the following section) is mapped by placing the SADA at a series of elevation and azimuthal angles, while maintaining a constant distance of 5 ft from the flap edge region.

6.2. Directivity

Fig. 24 shows the model with the flap-edge directivity contour mapped over a spherical surface, defined by the SADA positions. The measurements are for the flat edge flap model for $\alpha = 39^\circ$ and $M_0 = 0.17$. For the 6.3 kHz one-third octave frequency band shown, the directivity on the pressure side of the model is most intense "underneath" the model. This is the side that an

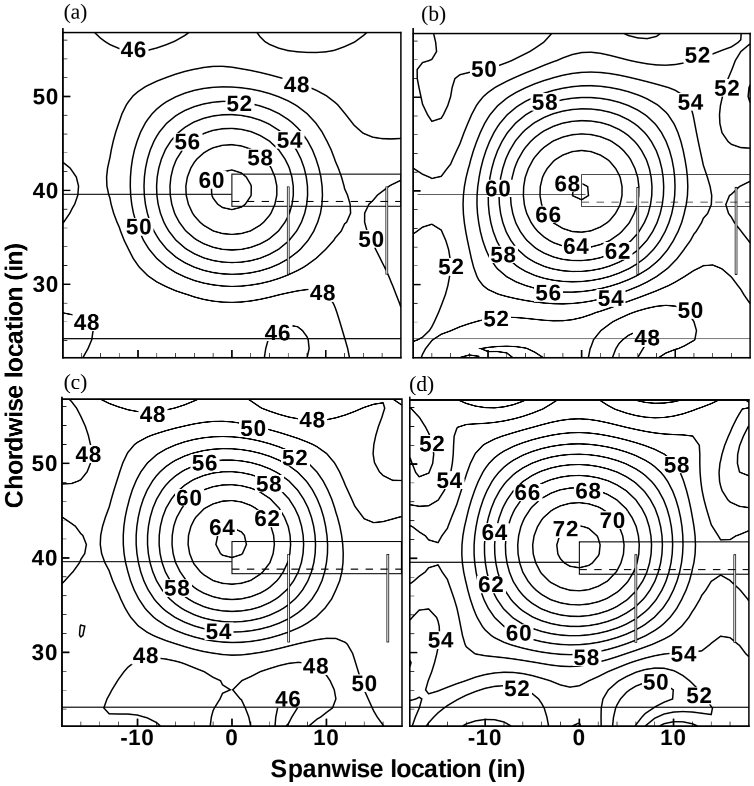

Fig. 23. Noise-source distribution contours over the flap-edge region using the SADA. $M_0 = 0.17$. One-third octave levels for $f_{1/3} = 12.5\,\text{kHz}$. The SADA position is $\theta = 107^\circ$ and $\phi = 0^\circ$. For the flat edge, the flap angles are (a) $\alpha = 29^\circ$ and (b) $\alpha = 39^\circ$. For the round edges, (c) $\alpha = 29^\circ$ and (d) $\alpha = 39^\circ$.

observer would “see” when an aircraft flies overhead. On the suction side of the model, the levels are less but are seen to increase in the downstream direction. Fig. 25 are pressure-side directivity maps for $\alpha = 29^\circ$ and 39° and selected frequencies ranging from 3.2 to 40 kHz. These maps are flattened versions of the spherical surfaces shown in Fig. 24, that are now viewed from the pressure side of the model. The positive azimuthal angles ψ are on the flap side of the model. The elevation angles ϕ with the smaller values (at the top of the plots) are in the downstream direction. For this flat flap-edge configuration, the directivities have a simple dipole-like shape at lower frequencies with the dipole axis oriented inline with angle ϕ at 90–107° and $\psi = 0^\circ$. For higher frequencies ($>12.5\,\text{kHz}$), the directivity levels are stronger on the side opposite the flap (ψ negative). This is contrary to that indicated by Eq. (21) for the thin-edge scatter cardioid-directivity modelling (with which, the stronger levels would be found for the flap side). The fact that the edge thickness is not small with respect to the acoustic wavelength at high frequencies, undoubtedly is a strong factor in this directivity result. At side angles away from $\psi = 0$, source region shielding and, alternately, reflection reinforcement from the flat side-edge surface can be expected to affect directivity. Still, this important result was not anticipated. The directivity for the flange edge is shown in Fig. 26, where at lower frequencies the levels and patterns are similar

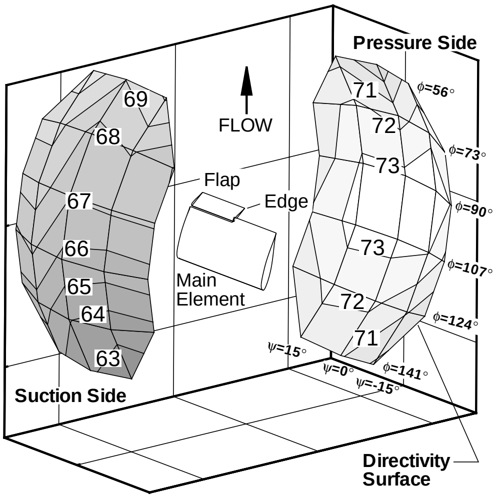

Fig. 24. Flap-edge noise directivity over 3-D "surface" defined by the SADA measurements. One-third octave levels for $f_{1/3} = 6.3\,\text{kHz}$.

to the flat edge results. However, at higher frequencies, the directivity patterns are somewhat more complicated and the levels are higher. Results for the round edge flap (see Fig. 27) are even more complicated with generally higher levels and multiple directional peaks–suggesting a more complex edge noise source (pressure scatter region of surface) than that found for the flat edge. With the application of grit to the pressure side of the round edge flap, the levels decrease to approximately those seen for the flat edge flap. However as Fig. 28 shows, the directivity remains just as complex as the round edge without grit.

6.3. Spectra and scaling

One-third octave spectra for the three flap configurations are shown in Fig. 29 for the SADA located at $\theta = 107^\circ$ and $\phi = 0^\circ$. The round edge is seen to be the loudest configuration at low frequencies but is the quieter at higher frequencies than both the flat and flanged edge flap. For the flanged edge flap, the broad spectral peak at higher frequencies is particularly strong (and thus troublesome). Fig. 30 shows spectra for different tunnel speeds for all three configurations, plus the flat and round edge configurations with grit applied. The spectral level dependence on tunnel speed is seen to be the most important, followed by flap angle and then by the application of grit. The grit serves to trip the boundary layers causing them (and thus the off-the-edge shear layers) to become more turbulent and thicker. Noise levels are reduced.

The spectra of Fig. 30 are scaled by normalizing the levels and frequencies with $M_{c_{AVG}}$ from Eq. (8) and δ from Eqs. (5) and (6) for the basic configurations, but from Eqs. (7) and (6) where grit is applied. Fig. 31 presents this scaling. The levels are referenced to the fifth power of the Mach number term. The levels are not taken to depend on δ. This normalization thus ignores a slight decrease in low-frequency noise found for the flat edge when grit is used, but is consistent with negligible change in low-frequency noise for the round edge when grit is used (see Fig. 30).

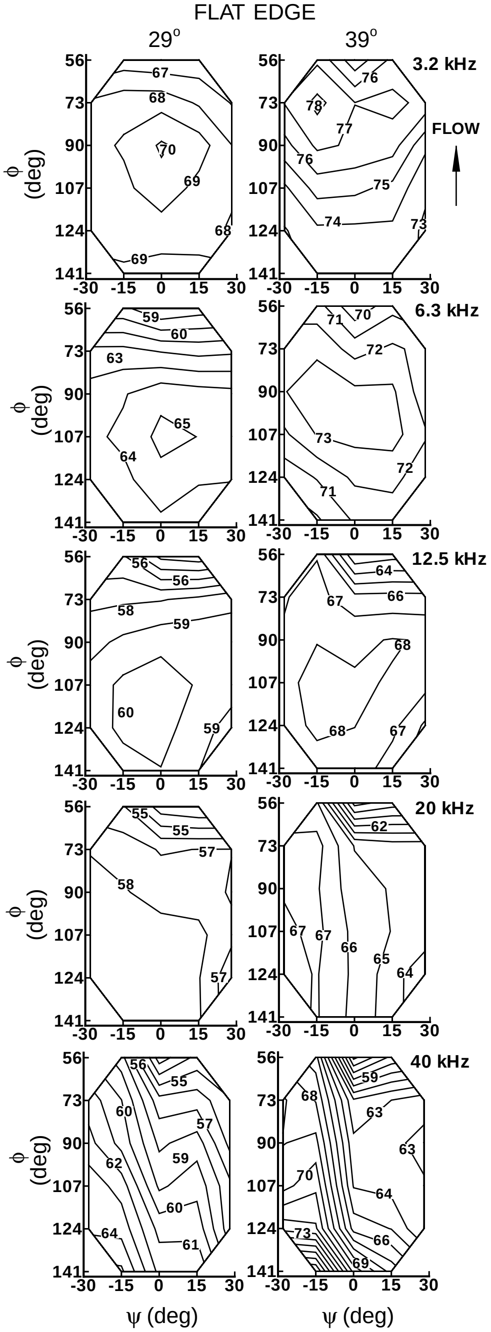

Fig. 25. Flap-edge noise directivity over projected surface for FLAT edge flap. $M_0 = 0.17$ and two flap angles ($\alpha = 29^\circ$ and 39°) for different one-third octave frequencies.

The primary effect of thickness δ is (taken as) to simply shift the noise levels to a lower frequency based on the Strouhal number $f_{1/3}\delta/U_{c_{AVG}}$. Note that the normalization brings the spectra for the flat edge, with and without grit, into good general agreement. However, there appears to be some

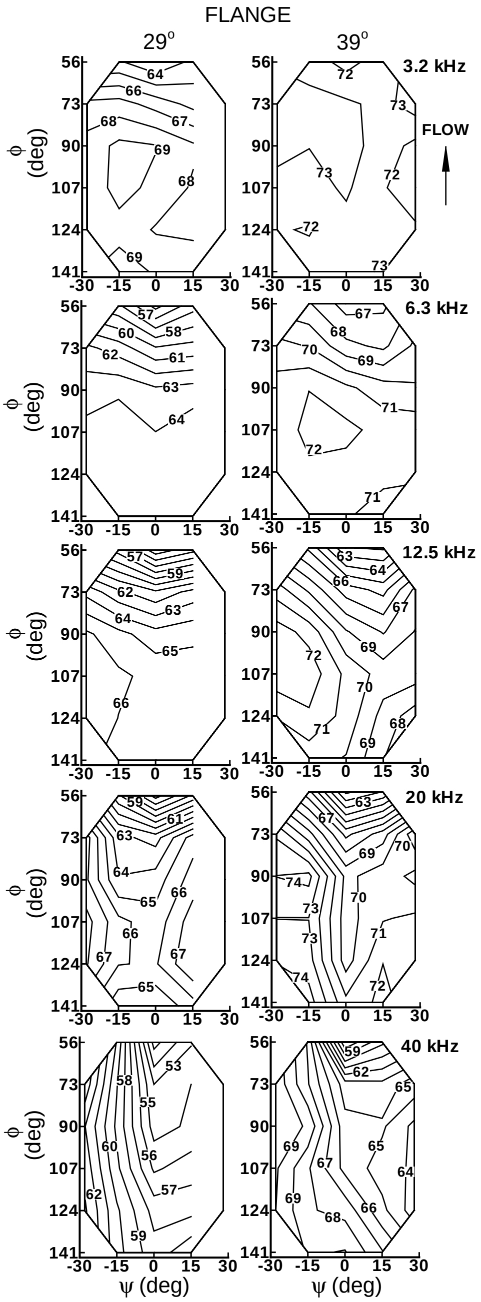

Fig. 26. Flap-edge noise directivity for flange edge flap for conditions of Fig. 25.

speed or Reynolds number dependence in spectral shape not accounted for. The normalization for the round edge is quite successful. The spectra data for the with- and without-grit cases appear well matched and coalesced. The spectral normalization for the flanged edge is also generally

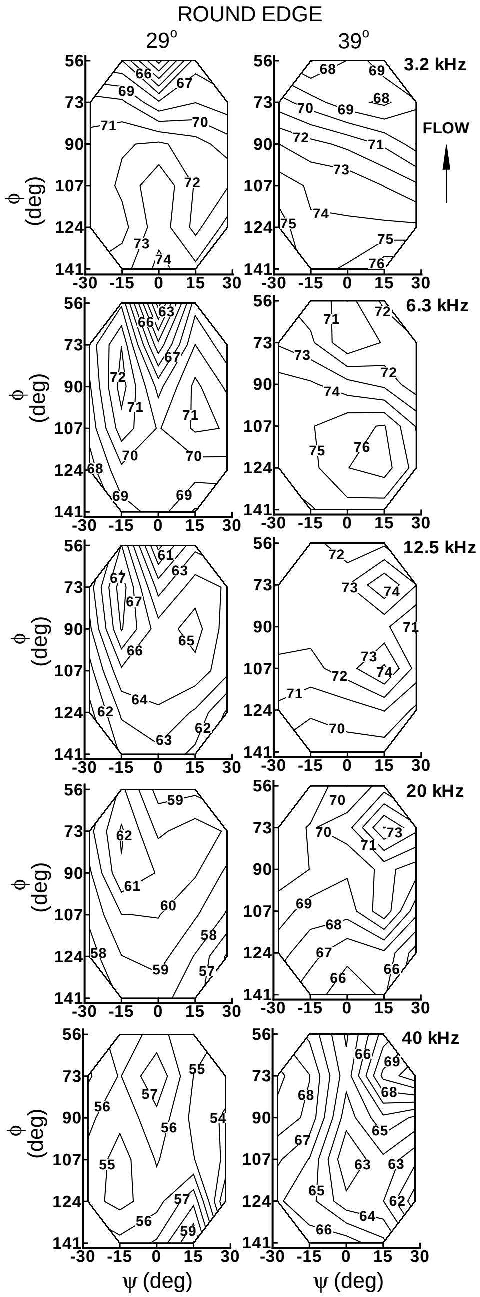

Fig. 27. Flap-edge noise directivity for ROUND edge flap for conditions of Fig. 25.

good. A lack of coalescence is seen over the broad high-frequency peak, likely related to the flange cavity. For all configurations, significant success is found in capturing the flap angle α dependence through the use of velocity $U_{c_{AVG}}$. Because this velocity depends on the flap C_N, it provides the appealing connection between noise and flap loading.

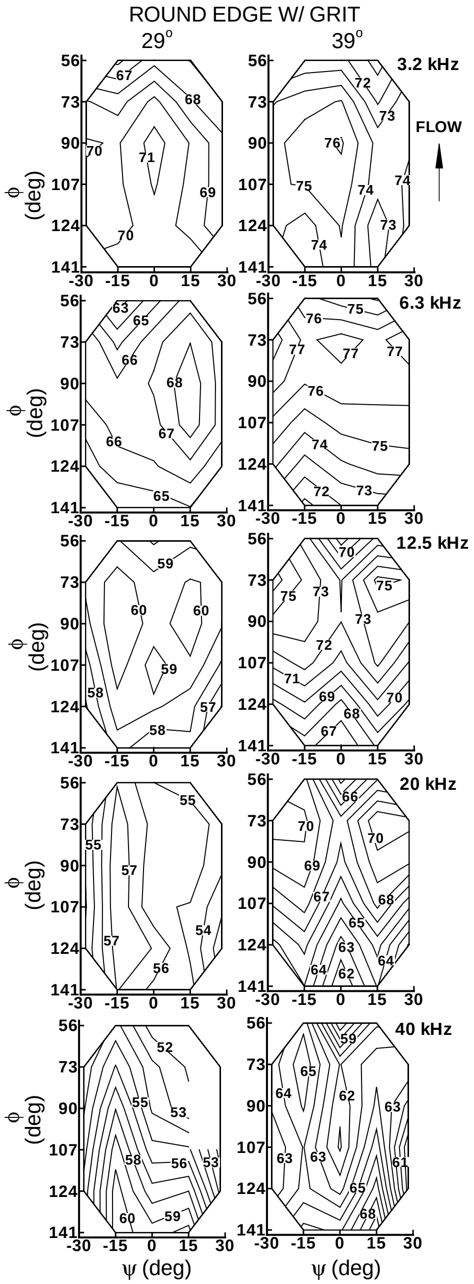

Fig. 28. Flap-edge noise directivity for ROUND edge flap with GRIT on surface for conditions of Fig. 25.

7. Conclusions

The flat (or blunt), flanged, and round geometries are flap-edge configurations in actual use on aircraft today. Spectra and directivity are presented for each to form the basis for semi-empirical

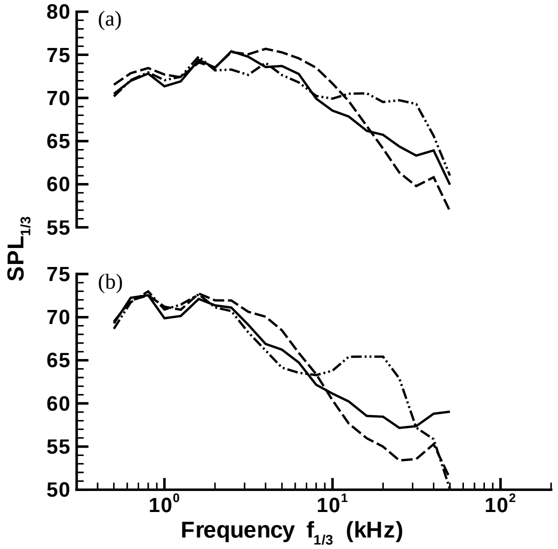

Fig. 29. Noise spectra for the flat, flange, and round edges for two flap angles at $M_0 = 0.17$. The flap angles are (a) $\alpha = 39°$ and (b) $\alpha = 29°$. The key is: ——, flat; – – –, round; ■■ – ■■, flange.

predictions. New scaling methods are given. Significantly, with some exceptions noted, the noise spectra for each edge configuration are very successfully scaled for flow speed, flap angles, and surface roughness, using the simplified flow and boundary-layer calculation methods developed herein. Of substantial significance are the directivity findings. For flat and flange edge flaps, a simple dipole directivity pattern is found for low frequencies and an approximate cardioid pattern is found, as expected, for high frequencies. But, contrary to that predicted from thin edge scatter theory, the cardioid pattern is reversed with the higher levels being found away from the extended flap side. This is explained as being related to edge thickness to acoustic wavelength effects. For rounded edges, more complex directivity patterns with multiple peaks are found.

This study also provides an experimental and theoretical validation that, for the flat flap-edge, shear layer instability and related pressure scatter is the dominant noise mechanism. For a higher flap angle, measured noise levels exceed predictions, which suggest additional contributions from surface sources that are not localized to just the immediate edge region. Such a de-localized source region is likely related to the vortex bursting that occurs at the higher angle. As with the flat edge, shear layer instability effects should be responsible for noise for the rounded flap edge, but the geometric features for the mechanism are different, producing different pressure scatter patterns and noise directivity. The flanged edge flap has an additional (and troublesome) high-frequency noise contribution, likely due to cavity-type effects.

Several newly applied diagnostic tools based on cross-spectra are used to determine the character of the hydrodynamic flow pressure field and the near-field noise. The noise generation distribution along the flap edge is determined. Two different noise prediction methods are developed and successfully validated from (1) a causality approach, utilizing cross-spectra between noise and surface pressures, and (2) an edge-noise scatter solution. Both methods use unsteady pressure data taken by sensors at the flat flap edge. A CFD flow solution is used as a

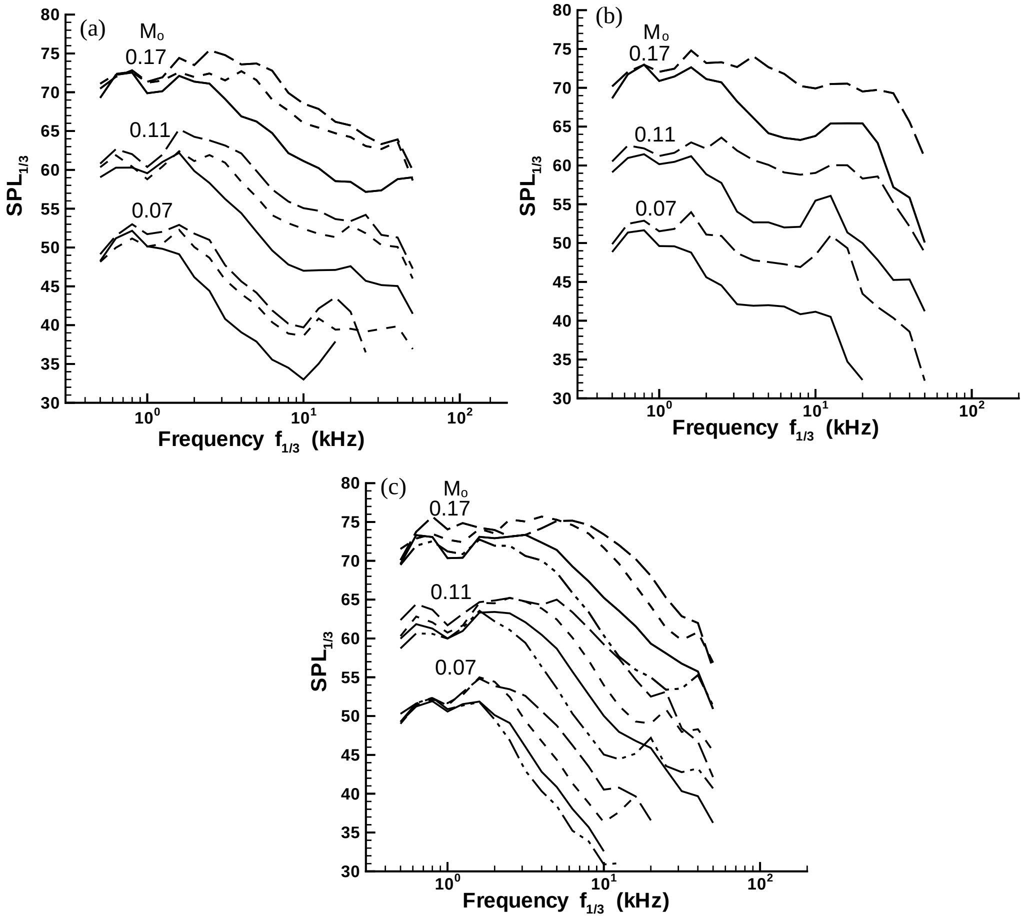

Fig. 30. Flap-edge noise spectra for (a) flat edge with/without grit, (b) flange edge, and (c) round edge with/without grit. The keys are as follows: ——, $\alpha = 29°$; —---—, $\alpha = 29°$ with grit; –––, $\alpha = 39°$; -----; $\alpha = 39°$ with grit.

guide for the basic flow pattern description, but simplified flow calculations provide the necessary boundary layer flow parameter inputs for the noise predictions and scaling. The predictions provide different but consistent theoretical bases for understanding the noise production at the edge.

Acknowledgements

The authors wish to gratefully acknowledge Daniel J. Stead of Lockheed-Martin for data processing, software development, and analysis. The authors also gratefully acknowledge Ron C. Verhapen of Wyle Laboratories for data acquisition system management and support.

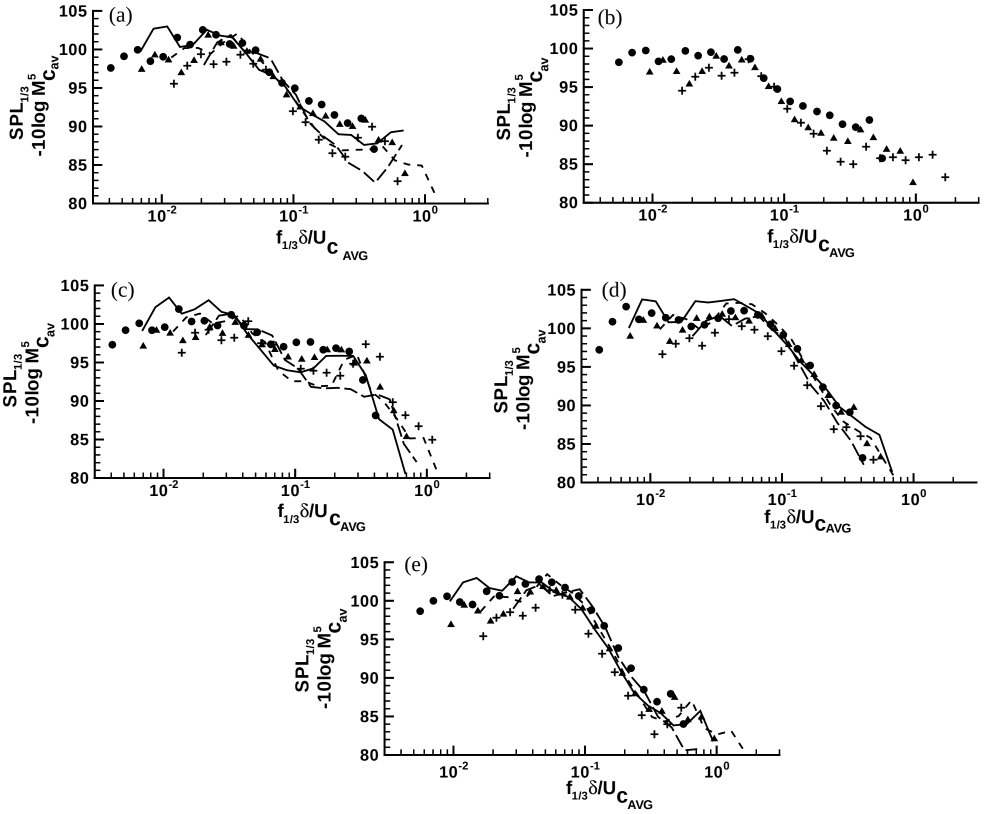

Fig. 31. Scaled flap-edge noise spectra for (a) flat edge, (b) flat edge with grit, (c) flange edge, (d) round edge, and (e) round edge with grit. For $\alpha = 29°$, the Mach numbers M_0 are: ——, 0.17; - - - -, 0.11; — — —, 0.07. For $\alpha = 39°$, the Mach numbers M_0 are: ● ● ●, 0.17; ▲▲▲, 0.11; + + +, 0.07.

Appendix A. Nomenclature

a_0	medium speed of sound
c	flap chordlength
C_N	normal force coefficient with respect to c
C_p	static pressure coefficient
COP_s	coherent output power spectrum of unsteady surface pressure with respect to farfield noise
d	distance from one sensor to another
D	directivity factor, Eq. (13)
$\mathrm{d}S(\mathbf{y})$	elemental surface area at $\mathbf{y}$
f	frequency
$f_{1/3}$	one-third octave band center frequency
Δf	spectrum frequency bandwidth

G_a	auto-spectrum of noise measured by SADA
G_s	auto-spectrum of unsteady surface pressure at sensor
$G_{a,s}$	cross-spectrum between outputs of SADA and surface pressure sensor
i	pressure sensor location number
j	$\sqrt{-1}$
k	acoustic wave number $(=\omega/a_0)$
ℓ_1	correlation length scale in chordwise edge direction
ℓ_3	correlation length scale in spanwise direction from edge
L	length of chordwise section that a sensor represents
L'	lift per unit span
M_c	convective Mach number, $(= U_c/a_0)$
$M_{c_{AVG}}$	average M_c, see Eq. (8).
M_0	tunnel Mach number, (U_0/a_0)
$\mathbf{n}$	normal vector to surface at $\mathbf{y}$
R_c	Reynolds number based on c and U_0
p_a	acoustic pressure time history
p_s	surface pressure time history
P_a	Fourier transform of p_a
P_s	Fourier transform of p_s
q_c	dynamic pressure based on convective speed U_c
q_0	tunnel dynamic pressure
r	distance $(=\|\mathbf{r}\|)$
r'	effective source-to-observer distance for quiescent field radiation, see Fig. 19
$\mathbf{r}$	vector distance $(=\mathbf{x}-\mathbf{y})$
$SADA$	small aperture directional array
t	time
u_{su}	inboard velocity along suction side
u_{pr}	inboard velocity along pressure side
u_v	velocity at radius r_0 from center of vortex, see Fig. 9(c)
U_c	convection velocity
U_h	hydrodynamic convection speed from the pressure to suction side, see Fig. 13
U_h'	hydrodynamic convection speed over the suction side, see Fig. 13
U_p	flow velocity at edge on pressure side, Eq. (4)
U_s	flow velocity at edge on suction side, Eq. (4)
U_0	tunnel velocity
x	chordwise distance from the flap leading edge
$\mathbf{x}$	noise observer location vector
$\mathbf{x}'$	effective observer location vector for radiation in quiescent field, see Fig. 19
y	spanwise distance from the flap edge
$\mathbf{y}$	surface noise source location vector
z	height above surface sensor, see Fig. 8
α	flap angle with respect to the main element
β_c	edge convective-flow skew angle, see Fig. 8
$\bar{\gamma}$	circulation density

$\gamma^2_{a,s}$	coherence function, see Eq. (9)
Γ	vortex circulation
δ	boundary-layer thickness
δ_0	boundary-layer thickness at airfoil zero angle of attack
ς	coherence decay factor for ℓ_3
η	coherence decay factor for ℓ_1
θ	angle between **n** and **x**, see Fig. 19
θ'	angle between **n** and **x'**, see Fig. 19
ϑ	observer azimuth angle defined for Eq. (21)
ρ	medium density
τ	retarded time, Eq. (12)
$\tau_{a,s}$	noise transmission time from sensor to SADA
ϕ	SADA elevation (flyover) angle, see Figs. 5 and 24
$\varphi_{a,s}$	cross-spectral phase between SADA and sensor outputs
ψ	SADA azimuth angle, see Fig. 24
ω	radian frequency $= 2\pi f$

References

[1] W.L. Willshire, D.G. Stephens, Aircraft noise technology for the 21th century, Noise-Con 98 Proceedings, Noise Control Foundation, Poughkeepsie, NY, 1998.

[2] D.G. Crighton, Airframe noise, in: H.H. Hubbard (Ed.), Aeroacoustics of Flight Vehicles: Theory and Practice: Noise Sources Vol. 1, Acoustical Society of America, Sewickley, PA, 1991, pp. 391–447.

[3] J.C. Hardin, Airframe self-noise–four years of research, NASA TMX-73908, 1976.

[4] M.R. Fink, Noise component method for airframe noise, Journal of Aircraft 16 (10) (1979) 659–665.

[5] M.R. Funk, R.H. Schlinker, Airframe noise component interaction studies, Journal of Aircraft 17 (2) (1980) 99–105.

[6] T.F. Brooks, T.H. Hodgson, Trailing edge noise prediction from measured surface pressures, Journal of Sound and Vibration 78 (1) (1981) 69–117.

[7] T.F. Brooks, M.A. Marcolini, Scaling of airfoil self-noise using measured flow parameters, American Institute of Aeronautics and Astronautics Journal 23 (2) (1985) 207–213.

[8] T.F. Brooks, M.A. Marcolini, D.S. Pope, Airfoil trailing edge flow measurements, American Institute of Aeronautics and Astronautics Journal 24 (8) (1986) 1245–1251.

[9] T.F. Brooks, M.A. Marcolini, Airfoil tip vortex formation noise, American Institute of Aeronautics and Astronautics Journal 24 (2) (1986) 246–252.

[10] T.F. Brooks, D.S. Pope, M.A. Marcolini, Airfoil self-noise and prediction, NASA RP 1218, 1989.

[11] P.J.W. Block, Assessment of airframe noise, Journal of Aircraft 16 (12) (1979) 834–841.

[12] J.M. Kendall, Measurements of noise produced by flow past lifting surfaces, American Institute of Aeronautics and Astronautics Paper 78-239, 1978.

[13] J.M. Kendall, W.F. Ahtye, Noise generation by a lifting wing/flap combination at reynolds numbers to, American Institute of Aeronautics and Astronautics Paper 80-0035, 1980.

[14] S.A. McInerny, W.C. Meecham, P.T. Soderman, Pressure fluctuations in the tip region of a blunt-tipped airfoil, American Institute of Aeronautics and Astronautics Journal 28 (1) (1990) 6–13.

[15] W.F. Ahtye, W.R. Miller, W.C. Meecham, Wing and flap noise measured by near- and far-field cross-correlation techniques, American Institute of Aeronautics and Astronautics Paper 79-0667, 1979.

[16] W.R. Miller, W.C. Meecham, W.F. Ahtye, Large scale model measurements of airframe noise using cross-correlation techniques, Journal of the Acoustical Society of America 71 (3) (1982) 591–599.

[17] M.G. Macaraeg, Fundamental investigations of airframe noise, American Institute of Aeronautics and Astronautics Paper 98-2224, 1998.

[18] P.H. Bent, W.C. Horne, M.E. Watts, Airframe noise scaling and source localization, Noise-Con 96 Proceedings, 1996, pp.145-150.

[19] J.A. Hayes, W.C. Horne, P.T. Soderman, P.H. Bent, Airframe noise characteristics of a 4.7% scale DC-10 model, American Institute of Aeronautics and Astronautics Paper 97-1594, 1997.

[20] Y.P. Guo, B.A. Hardy, P.H. Bent, K. Yamamoto, M.C. Joshi, Noise characteristics of DC-10 aircraft high lift system, NASA CR CRAD-9310-TR-4893, 1998.

[21] Y.P. Guo, P.H. Bent, K. Yamamoto, M.C. Joshi, Surface pressure fluctuations on DC-10 high lift system and their correlation with far field noise, NASA CR CRAD-9310-TR-4872, 1998.

[22] Y.P. Guo, Modeling of noise reduction by flap side edge fences, NASA CR CRAD-9402-TR-5767, 1999.

[23] B.L. Storms, T.T. Takahashi, J.C. Ross, Aerodynamic influence of a finite-span flap on a simple wing, SAE Paper 95-1977, 1995.

[24] C.F. Horne, J.A. Hayes, J.C. Ross, Measurements of unsteady pressure fluctuations on the surface of an unswept multi-element airfoil, American Institute of Aeronautics and Astronautics Paper 97-1645, 1997.

[25] B.L. Storms, J.C. Ross, C.F. Horne, J.A. Hayes, R.P. Dougherty, J.R. Underbrink, D.F. Scharpf, P.J. Mariarty, An aeroacoustic study of an unswept wing with a three-dimensional high-lift system, NASA TM 1998-112222, 1998.

[26] M.R. Khorrami, B.A. Singer, M.A. Takallu, Analysis of flap side-edge flowfield for identification and modeling of possible noise sources, SAE Paper 971917, 1997.

[27] R.H. Radezrsky, B.A. Singer, M.R. Khorrami, Detailed measurements of a flap side-edge flow field, American Institute of Aeronautics and Astronautics Paper 98-0700, 1998.

[28] M.R. Khorrami, B.A. Singer, R.H. Radezrsky, Reynolds-averaged navier-stokes computations of a flap side-edge flow field, American Institute of Aeronautics and Astronautics Paper 98-0768, 1998.

[29] M.A. Takallu, K.R. Laflin, Reynolds-averaged navier-stokes simulations of two partial-span flap wing experiments, American Institute of Aeronautics and Astronautics Paper 98-0701, 1998.

[30] C.L. Streett, Numerical simulation of fluctuations leading to noise in a flap-edge flowfield, American Institute of Aeronautics and Astronautics Paper 98-0628, 1998.

[31] M.R. Khorrami, B.A. Singer, Stability analysis for noise-source modeling of a part-span flap, American Institute of Aeronautics and Astronautics Paper 98-2225, 1998.

[32] Y.P. Guo, A semi-analytical/semi-empirical model for flap side edge noise prediction, NASA CR CRAD-9310-TR-3765, 1998.

[33] Y.P. Guo, Prediction of flap side edge noise, American Institute of Aeronautics and Astronautics Paper 99-1804, 1999.

[34] K.R. Meadows, T.F. Brooks, W.M. Humphreys, W.W. Hunter, C.H. Gerhold, Aeroacoustic measurements of a wing-flap configuration, American Institute of Aeronautics and Astronautics Paper 97-1595, 1997.

[35] W.M. Humphreys, T.F. Brooks, W.W. Hunter, K.R. Meadows, Design and use of microphone directional arrays for aeroacoustic measurements, American Institute of Aeronautics and Astronautics Paper 98-0471, 1998.

[36] T.F. Brooks, W.M. Humphreys, Effect of directional array size on the measurement of airframe noise components, American Institute of Aeronautics and Astronautics Paper 99-1958, 1999.

[37] R.K. Amiet, Refraction of sound by a shear layer, Journal of Sound and Vibration 58 (3) (1978) 467–482.

[38] T.F. Brooks, M.A. Marcolini, D.S. Pope, Adirectional array approach for the measurement of rotor noise source distributions with controlled spatial resolution, Journal of Sound and Vibration 112 (1) (1987) 192–197.

[39] M.A. Marcolini, T.F. Brooks, Rotor noise measurement using a directional microphone array, Journal of the American Helicopter Society 37 (2) (1992) 11–22.

[40] A.M. Kuethe, C.-Y. Chow, Foundations of Aerodynamics: Bases of Aerodynamic Design, 3rd edition, Wiley, New York, 1976.

[41] W. Johnson, Helicofter Theory, Princeton University Press, Princeton, NJ, 1980.

[42] T.F. Brooks, D.D. Boyd Jr., C.L. Burley, J.R. Jolly Jr., Aeroacoustics codes for rotor harmonic and BVI noise – CAMRAD.Mod1/HIRES, Journal of the American Helicopter Society 45 (2) (2000) 63–79.

[43] J.E. Ffowcs Williams, D.L. Hawkings, Sound generation by turbulence and surfaces in arbitrary motion, Philosphical Transactions of Royal Society London A 264 (1151) (1969) 321–342.

[44] J.S. Bendat, A.G. Piersol, Engineering Applications of Correlation and Spectral Analysis (2nd Edition, 1993), Wiley, New York, 1980.

[45] T.E. Siddon, Surface dipole strength by a cross-correlation method, Journal Acoustical Society of America 53 (2) (1973) 619–633.

[46] N. Curle, The influence of solid boundaries upon aerodynamic sound, Proceedings of the Royal Society (London) A 231 (1955) 505–514.

[47] M.S. Howe, A review of the theory of trailing edge noise, Journal of Sound and Vibration 61 (1978) 437–465.